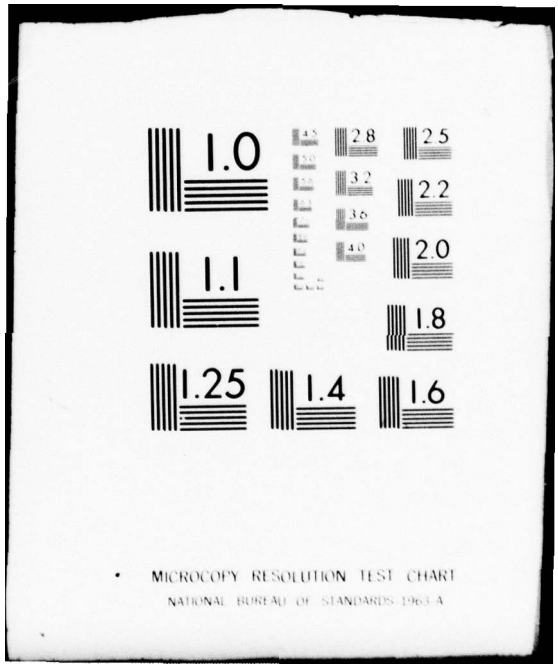
AD-A068 972 CERAMIC FINISHING CO STATE COLLEGE PA F/G 11/2
LOCALIZED IMPACT DAMAGE IN CERAMICS. THEORY OF ELASTIC-PLASTIC --ETC(U)
JAN 79 H P KIRCHNER, D M RICHARD, R C GARVIE N00014-74-0241
UNCLASSIFIED NL

1 OF 2
AD A068972




1.0
1.1
1.25
1.4
1.6
2.8
3.2
3.6
4.0
2.5
2.2
2.0
1.8
MICROCOPY RESOLUTION TEST CHART
NATIONAL BUREAU OF STANDARDS 1963-A

LEVEL II
A050 357

AD A068972

Ceramic Finishing Company
State College, Pennsylvania 16801

(9) Technical rept. no. 7, 1 Feb 78 - 31 Jan 79

TECHNICAL REPORT NO. 7

(6)

LOCALIZED IMPACT DAMAGE IN CERAMICS.

Theory of Elastic-Plastic Impact on Ceramics
Localized Impact Damage in Transformation Toughened Zirconia.
Crack Propagation and Branching in Transformation Toughened Zirconia.

DDC FILE COPY

DDC
MAY 24 1979
C

(11) January, 1979

(12) 109p.

(10) Prepared By
H. P. Kirchner,
D. M. Richard,
R. C. Garvie*
R. M. Gruver
* CSIRO, Melbourne

(15)

Prepared under Contract No. N00014-74-0241 for the
Office of Naval Research, Department of the Navy
Requisition No. NR032-545/12-17-73(471)

Distribution of this document is unlimited

404 419
79 05 21 027

REPORT DOCUMENTATION PAGE

READ INSTRUCTIONS BEFORE COMPLETING FORM

1. REPORT NUMBER
2. GOVT ACCESSION NO.
3. RECIPIENT'S CATALOG NUMBER

4. TITLE (and Subtitle)
Localized Impact Damage in Ceramics

5. TYPE OF REPORT & PERIOD COVERED
Technical Report
Feb. 1, 1978-Jan. 31, 1979

6. PERFORMING ORG. REPORT NUMBER
N00014-74-C-0241

7. AUTHOR(s) H. P. Kirchner
D. M. Richard
R. C. Garvie (CSIRO, Melbourne)
R. M. Gruver

8. CONTRACT OR GRANT NUMBER(s)

9. PERFORMING ORGANIZATION NAME AND ADDRESS
Ceramic Finishing Company
P.O. Box 498
State College, PA 16801

10. PROGRAM ELEMENT, PROJECT, TASK AREA & WORK UNIT NUMBERS

11. CONTROLLING OFFICE NAME AND ADDRESS
Office of Naval Research
Department of the Navy
Arlington, VA 22217

12. REPORT DATE
January 1979

13. NUMBER OF PAGES
105

14. MONITORING AGENCY NAME & ADDRESS(if different from Controlling Office)
Distribution of this document is unlimited

15. SECURITY CLASS. (of this report)
Unclassified

15a. DECLASSIFICATION/DOWNGRADING SCHEDULE

16. DISTRIBUTION STATEMENT (of this Report)

This document has been approved for public release and sale; its distribution is unlimited.

17. DISTRIBUTION STATEMENT (of the abstract entered in Block 20, if different from Report)

18. SUPPLEMENTARY NOTES

19. KEY WORDS (Continue on reverse side if necessary and identify by block number)
ceramics, glass, zirconia, transformation toughening, localized impact damage, Hertzian cone crack, radial crack, lateral vent crack, stress waves, energy loss mechanisms, mechanical impedance, crack branching, fracture mirror, stress intensity factor, impact load, penetration, strength, strength degradation

20. ABSTRACT (Continue on reverse side if necessary and identify by block number)
The following are covered in this report:
(1) Theory of elastic-plastic impact on ceramics;
(2) Localized impact damage in transformation toughened zirconia;
(3) Crack propagation and branching in transformation toughened zirconia.

404 419

DD FORM 1 JAN 73 1473 EDITION OF 1 NOV 65 IS OBSOLETE

Ceramic Finishing Company
State College, Pennsylvania 16801

TECHNICAL REPORT NO. 7

LOCALIZED IMPACT DAMAGE IN CERAMICS

Theory of Elastic-Plastic Impact on Ceramics
Localized Impact Damage in Transformation Toughened Zirconia
Crack Propagation and Branching in Transformation Toughened Zirconia

January, 1979

Prepared by

H. P. Kirchner
D. M. Richard
R. C. Garvie*
R. M. Gruver
*CSIRO, Melbourne

Prepared under Contract No. N00014-74-0241 for the
Office of Naval Research, Department of the Navy
Requisition No. NR032-545/12-17-73(471)

Distribution of this document is unlimited

Table of Contents

Report of Documentation Page i

Title Page ii

Theory of Elastic-Plastic Impact on Ceramics 1

Localized Impact Damage in Transformation Toughened Zirconia 43

Crack Propagation and Branching in Transformation Toughened Zirconia 75

ACCESSION for
NTIS White Section
DDC Buff Section
UNANNOUNCED
JUSTIFICATION
BY
DISTRIBUTION/AVAILABILITY CODES
Dist. SPECIAL
A

Theory of Elastic-Plastic Impact on Ceramics

by

D. M. Richard
H. P. Kirchner

August, 1978

Ceramic Finishing Company
P.O. Box 498
State College, PA 16801

ABSTRACT

Theoretical relationships describing characteristics of elastic-plastic impact by rigid spheres on flat plates were derived. The theory is based on simple empirical laws relating the pressure (η) to the size of the indentation or contact. The derivation neglected the stress wave energy. With the aid of conservation and fracture mechanics relations, equations were derived for the important impact characteristics including depth of damage, remaining strength and coefficient of restitution. The theory includes the equations of Evans , and Wiederhorn and Lawn which appear as special cases.

The theory was evaluated by comparison with experimental data obtained using the following combinations of materials:

Target	Impacting spheres
Transformation toughened zirconia	Tungsten carbide
Zinc sulfide	Glass
Glass	Glass

The responses of the first two material combinations were elastic-plastic while the third was elastic. Agreement with the theory was reasonable for elastic-plastic impacts on transformation toughened zirconia and zinc sulfide but for elastic impacts on glass, experimental difficulties prevented the comparisons except for the contact radii, so that further investigation is required.

I. INTRODUCTION

Presently available theories of solid-solid impact are based mainly on the Hertz theory of contact.[1] Evans[2,3] used the Hertz theory to calculate the load at various impact velocities and combined this result with fracture mechanics relations to obtain predictions of the depth of damage and strength degradation for impacts of spheres on flat plates. Similarly, Timoshenko and Goodier[4] derived an expression for the contact time of elastic spheres impacting at various velocities. They assumed that the contact time was large compared with the natural vibration frequency of the spheres so that these vibrations could be neglected. Yoh-Han Pao[5] extended the application of the Hertz theory to impact of small viscoelastic spheres on a steel plate. Evans[6] and Wiederhorn and Lawn[7] have derived expressions for the elastic-plastic regime and impact by sharp particles.

In this paper, a theory of elastic-plastic impact by rigid spheres on flat plates is derived. The theory is based on an empirical law relating the pressure to the size of the indentation and contact. The impact response was determined for three combinations of ceramic materials and the results were compared with theoretical predictions. Lastly, the effect of variations in impact conditions was evaluated by qualitative methods.

Several definitions are necessary. Various stages of impact are illustrated in Figure 1. At first contact the velocity of the impacting sphere is the impact velocity (V_o). As the sphere moves into the target it decelerates and comes to rest as shown in Figure 1(B). The maximum distance that the sphere moves into the target is the maximum penetration (z_c). At this

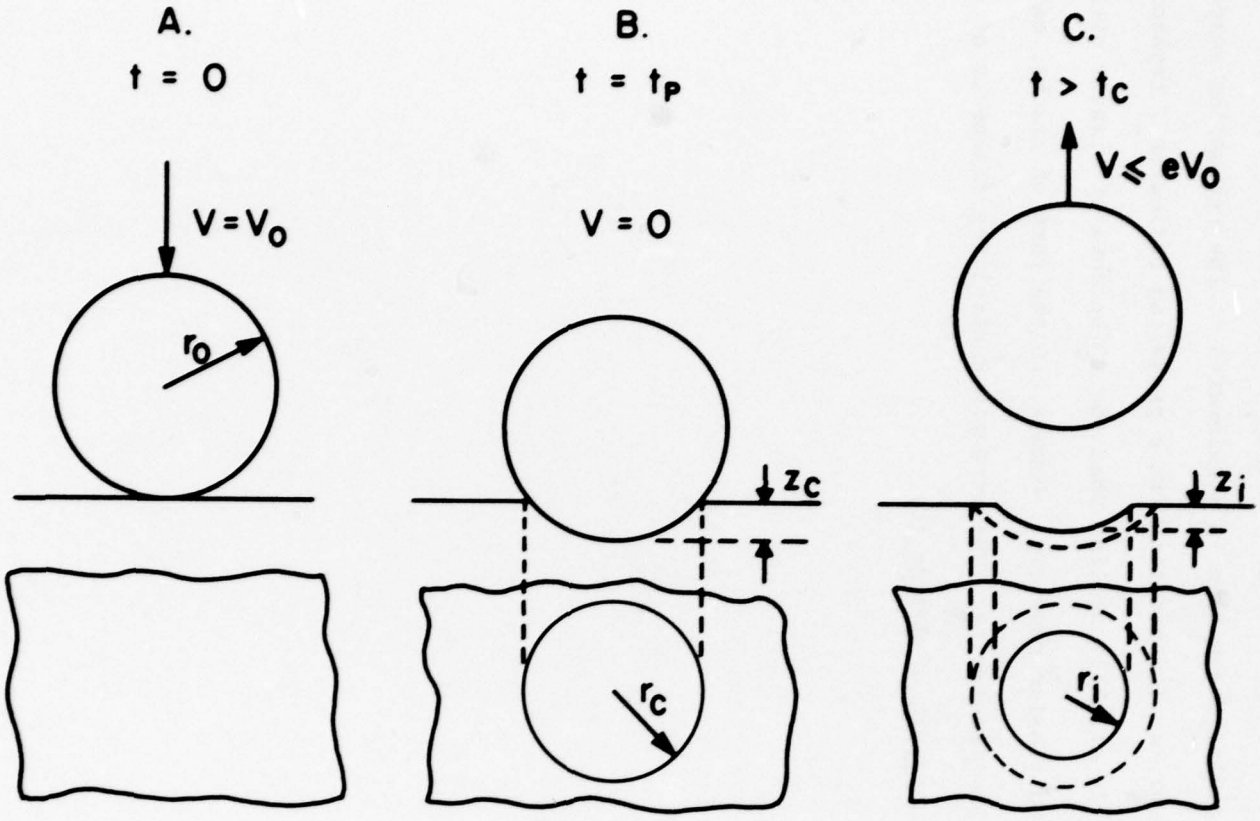


Fig.1. A. At $t=0$, the impacting particle contacts the target at $V=V_0$. During Phase I the particle penetrates the target to a depth z_c (ie a radius of contact r_c), at that time (t_p) its velocity is zero. C. During Phase II of the impact the target recovers elastically, the particle leaves the target with a velocity less than the impact velocity, and may leave an indentation of radius r_i.

point the radius of contact between the sphere and the target is the maximum contact radius (r_c) and the force is a maximum called the load (P). As elastic recovery occurs, the sphere is accelerated to the rebounding velocity. After elastic recovery an indentation with a projected radius (r_i) remains in the target. r_i is slightly smaller than the r_c because of elastic strain at the periphery and elastic recovery. Damage, in the form of cracks, may have spread from the impact site. The strength controlling dimension of this damage is called the depth of damage (c).

II. THEORY OF ELASTIC-PLASTIC IMPACT

Impact conditions and characteristics are listed in Table I. In this paper impact characteristics are derived for perpendicular impacts by rigid spheres on flat plates at subsonic velocities. The stress waves generated by impact are neglected. The derivation is based on an expression for the pressure of indentation based on the following empirical law*:

$$\eta' = \kappa' \left(\frac{r_i}{r_o}\right)^{\xi'} \tag{1}$$

in which κ' is a constant for a particular combination of sphere and plate expressed in units of pressure and ξ' is the slope of the curve of $\log \eta' = \log \kappa' + \xi' \log\left(\frac{r_i}{r_o}\right)$ as in Meyer's analysis[8,9] of hardness test data. κ' and ξ' are considered to be the resistance to indentation and an exponent, perhaps related to work hardening, respectively. There is a similar assumed relationship between the pressure of contact and the radius of contact

$$\eta = \kappa \left(\frac{r_c}{r_o}\right)^{\xi} \tag{2}$$

This expression takes account of both the elastically deformed rim around the indentation and the indentation itself and κ and ξ are characteristics of both the elastic and plastic deformation.

---

*See List of Symbols, Table II.

TABLE I

Impact Conditions and Characteristics

Impact Conditions

Account for or neglect stress waves
Blunt projectile (sphere or punch) or sharp projectile (cone or pyramid)
Angle of impact
Deformable or rigid projectile
Subsonic or transsonic velocity
Single particle or multiple particles

Impact Characteristics

Phase I	Phase II
Impact velocity	Coefficient of restitution
Radius of contact	Radius of indentation (load)
Load	
Time of penetration	Time of elastic recovery (lateral vent crack size)
Depth of damage	
Remaining strength	(remaining strength)

TABLE II

-List of Symbols-

a	Diagonal dimension of contact of a regular four sided pyramidal indenter (Vickers indenter)
b	Diagonal of a regular four sided pyramidal indenter
c	Depth of damage
c_0	Velocity of longitudinal waves of infinite wavelength in a bar made of the same material as the target, $c_0 = (E/\rho)^{\frac{1}{2}}$
c_{10}	Velocity of longitudinal waves of infinite wavelength in a bar made of the same material as the projectile, $c_{10} = (E_1/\rho_1)^{\frac{1}{2}}$
e	Coefficient of restitution
E	Young's modulus of the target material
E_1	Young's modulus of the projectile material
$F_0(\zeta)$	$= (2\zeta^2 - \gamma^2)^2 - 4\zeta[(\zeta^2 - 1)(\zeta^2 - \gamma^2)]^{\frac{1}{2}}$
g	$= [\frac{1-\sigma^2}{E} + \frac{1-\sigma_1^2}{E_1}]$
H	Vicker's hardness
$J\{\cdot\}$	Imaginary part of the complex number $\{\cdot\}$
K_{IC}	Critical stress intensity factor of the target
M	Mass of the projectile
P	Load developed during impact
r	Radius of contact at time t ($r = \int_0^t r(t)\, dt$)
r_0	Radius of a spherical projectile
r_c	Maximum radius of contact
r_i	Radius of Indentation
t_e	Time of elastic deformation (penetration)
t_p	Time of elastic/plastic deformation (penetration)
$t_{e\ell}$	Time of elastic Recovery
$t_{p\ell}$	Time of plastic deformation

TABLE II (Continued)

t_c	Time of contact between target and projectile
V	Instantaneous velocity
V_0	Impact velocity
W	Energy at time t ($W = \int_c^t W(t)\, dt$)
W_p	Energy of penetration
$W_{p\ell}$	Plastic energy
$W_{e\ell}$	Elastic energy
W_s	Stress wave energy
Y	Constant characteristic of the geometry of a crack
z	Penetration at time t ($z = \int_o^t z(t)dt$)
z_o	Length of a conical or a pyramidal indenter
z_c	Maximum penetration
z_i	Depth of indentation
α	Half angle of a conical or pyramidal indenter
β	Angle of incidence of a projectile on a plate
γ	$= \sqrt{\frac{2(1-\sigma)}{1-2\sigma}}$
ζ	Dummy variable for integration
η	Pressure of contact
η'	Pressure of indentation
κ	Resistance to penetration
κ'	Resistance to indentation
$\hat{\lambda}$	$= \frac{2\tau\, M^{-1/5}\, r_o^{3/5}\, g^{-6/5}}{\rho\, c_o^3}$

TABLE II (Continued)

λ	$= \hat{\lambda}(1 + \frac{\rho_1 c_{o1}}{\rho c_o}) = \hat{\lambda}(1 + \sqrt{\frac{\rho_1 E_1}{\rho E}})$
ξ	Exponent characteristic of the variation of the pressure of contact with increasing load
ξ'	Exponent related to work hardening
ρ	Density of the target
ρ_1	Density of the projectile
σ	Poisson's ratio of the target
σ_1	Poisson's ratio of the projectile
σ_F	Fracture stress
τ	$= (1.068)^5 \ (1+\sigma) \ (\frac{1-\sigma}{1-2\sigma}) \ (\frac{16}{15})^{6/5} \times J\{ \int_o^\infty \frac{(\zeta^2-1)^{\frac{1}{2}} \zeta \, d\zeta}{F_o(\zeta)} \}$
χ	Geometrical "constant" characteristic of the contact
Ω	$= \kappa \pi r_o^2 \ [\frac{2}{3} \rho_1 \frac{(\xi+4)}{\kappa}] \frac{\xi+2}{\xi+4}$

As in Meyer's law the pressure of contact is assumed to equal the load divided by the projected contact area leading to*

$$P = \kappa \pi r_o^2 \left(\frac{r_c}{r_o}\right)^{\xi+2} \tag{3}$$

Experimental evidence of the applicability of equation (1) to ceramics has been presented by Evans and Wilshaw[3] for static indentations in zinc sulfide and by Kirchner et al[10] for transformation toughened zirconia ($TTZrO_2$). The data at the larger contact radii are more reliable than those at smaller contact radii so the slopes were based mainly on the more reliable part of the data.

Assuming that the stress wave energy is negligible, the work done by the impact load during penetration is equal to the incoming kinetic energy, so that

$$M V \, dV = P(z) \, dz$$

or

$$\tfrac{1}{2} M V_0^2 = \int_0^{z_c} \kappa \pi r_o^2 \left(\frac{2z}{r_o}\right)^{\frac{\xi+2}{2}} dz \tag{4}$$

which when integrated yields

$$\tfrac{1}{2} M V_o^2 = \frac{\kappa \pi r_o^3}{\xi+4} \left(\frac{r_c}{r_o}\right)^{\xi+4} \tag{5}$$

Rearranging (5) yields a relation for radius of contact in terms of impact velocity

---

*We are mainly interested in the maximum load. However, as the load increases after initial contact, P is related to the instantaneous radius of contact (r) by $P = \kappa \pi r_o^2 \left(\frac{r}{r_o}\right)^{\xi+2} = \kappa \pi r_o^2 \left(\frac{2z}{r_o}\right)^{\frac{\xi+2}{2}}$.

$$r_c = r_o \left[\tfrac{1}{2} \frac{M(\xi+4)}{\kappa \pi r_o^3} V_o^2\right]^{\frac{1}{\xi+4}} \tag{6}$$

which when substituted in (3) yields an expression for the load

$$P = \kappa \pi r_o^2 \left[\tfrac{1}{2} \frac{M(\xi+4)}{\kappa \pi r_o^3}\right]^{\frac{\xi+2}{\xi+4}} V_o^{2\frac{\xi+2}{\xi+4}} \tag{7}$$

Then, by substituting Ω for the terms not involving the velocity, equation (7) can be shortened to

$$P = \Omega V_o^{\frac{2(\xi+2)}{(\xi+4)}} \tag{8}$$

The following fracture mechanics relation[11]

$$K_{IC} = \chi \frac{P}{c^{3/2}} \tag{9}$$

describing the variation of the depth of damage with the load for solid-solid contacts in which χ is a "constant" for a particular combination of plate and indenter, accounting for effects related to indenter shape, interface friction, etc., was substituted in (8) to obtain the following expression for the depth of damage

$$c = \left(\frac{\chi \Omega}{K_{IC}}\right)^{2/3} V_o^{\frac{4}{3}\left(\frac{\xi+2}{\xi+4}\right)} \tag{10}$$

Assuming a uniform tensile stress is applied during subsequent use of the damaged member so that the fracture stress is described by

$$K_{IC} = Y \sigma_F c^{1/2} \tag{11}$$

the expression for the remaining strength after impact damage was obtained by using equation (11) to substitute for c in equation (10) with the following result

$$\sigma_F = \frac{K_{IC}^{4/3}}{Y(\chi\Omega)^{1/3}\, V_0^{\frac{2}{3}(\frac{\xi+2}{\xi+4})}} \tag{12}$$

Then, using the principle that the impulse equals the change in momentum, the time of penetration was determined using

$$dt = \frac{M}{P}\, dV = \frac{M}{\Omega}\, \frac{dV}{V^{2(\frac{\xi+2}{\xi+4})}} \tag{13}$$

which after integration yields

$$t_p = \left|\left(\frac{\xi+4}{\xi}\right)\right| \left(\frac{M}{\Omega}\right)\, V_o^{-\frac{\xi}{\xi+4}} \tag{14}$$

Note that the time of penetration is zero at infinite velocity so that the constant of integration is zero.

Now considering the second phase of the impact process in which elastic recovery occurs, expressions for the coefficient of restitution, the rebounding velocity and the time for elastic recovery can be derived. Starting from equation (1) we obtain

$$P = \kappa' \pi r_o^2 \left(\frac{r_i}{r_o}\right)^{\xi'+2} \tag{15}$$

which is similar to equation (3). The energy of penetration to the radius r is, from equation (5)

$$W = \frac{\kappa \pi r_0^3}{\xi+4} \left(\frac{r}{r_o}\right)^{\xi+4} \tag{16}$$

and the total energy of penetration is

$$W_p = \frac{\kappa \pi r_o^3}{\xi+4} \left(\frac{r_c}{r_o}\right)^{\xi+4} \tag{17}$$

while the energy of plastic deformation is

$$W_{p\ell} = \frac{\kappa \pi r_o^3}{\xi+4} \left(\frac{r_i}{r_o}\right)^{\xi+4} \tag{18}$$

and the difference between equation (17) and (18) is the elastic energy

$$W_{e\ell} = \frac{\kappa \pi r_o^3}{\xi+4} \left[\left(\frac{r_c}{r_o}\right)^{\xi+4} - \left(\frac{r_i}{r_o}\right)^{\xi+4}\right] \tag{19}$$

To eliminate r_i, equation (19) was written as

$$W_{e\ell} = \frac{\kappa \pi r_o^3}{\xi+4} \left(\frac{r_c}{r_o}\right)^{\xi+4} \left[1 - \left(\frac{r_i}{r_c}\right)^{\xi+4}\right]$$

and an expression for r_i was obtained combining (3) and (15)

$$\frac{r_i}{r_c} = \left[\left(\frac{\kappa}{\kappa'}\right) \left(\frac{r_c}{r_o}\right)^{\xi-\xi'}\right]^{\frac{1}{\xi'+2}}$$

yielding

$$W_{e\ell} = \frac{\kappa \pi r_0^3}{\xi+4} \left(\frac{r_c}{r_o}\right)^{\xi+4} \left\{1 - \left[\left(\frac{\kappa}{\kappa'}\right)\left(\frac{r_c}{r_o}\right)^{\xi-\xi'}\right]^{\frac{\xi+4}{\xi'+2}}\right\}. \tag{20}$$

Using the fact that

$$W_{e\ell} = W_p - W_{p\ell}$$

and that the coefficient of restitution squared is equal to the ratio of the elastic energy to the impact energy so that

$$e^2 = \frac{W_{e\ell}}{W_p} = 1 - \frac{W_{p\ell}}{W_p}$$

and noting that the first term in the right of equation (20) is the impact energy (equation 17), e^2 can be obtained by dividing $W_{e\ell}$ in equation (20) by W_p and substituting for r_c using equation (6) to obtain

$$e = \left\{1 - \left(\frac{\kappa}{\kappa'}\right)^{\frac{\xi+4}{\xi'+2}} \left[\frac{M(\xi+4)}{2\kappa\pi r_o^3}\right]^{\frac{\xi-\xi'}{\xi'+2}} V_o^{\frac{2(\xi-\xi')}{\xi'+2}}\right\}^{\frac{1}{2}} \tag{21}$$

The above equation accounts for extreme variations in material properties. For elastic materials, there is no indentation. In that case r_i tends toward zero so that κ' tends toward infinity and $e = 1$ as would be expected when stress waves are neglected. For perfectly plastic materials κ and κ' are equal so the first term to the right of the minus sign is one. Also, ξ and ξ' are equal so that the exponents of the remaining terms are zero so that these terms are equal to one. Therefore, for the perfectly plastic case $e = 0$, as would be expected when there is no elastic recovery.

If one assumes that the plastic deformation occurs before the elastic deformation, rather than the reverse, one can determine the time of plastic deformation by integrating equation (13) over the range of velocities from the impact velocity to the rebounding velocity with the following result

$$t_{p\ell} = \left|\frac{\xi+4}{\xi}\right| \frac{M}{\Omega} \left[(eV_o)^{-\frac{\xi}{\xi+4}} - V_o^{-\frac{\xi}{\xi+4}}\right] \tag{22a}$$

Then the time for elastic recovery is given by

$$t_{e\ell} = t_p - t_{p\ell}$$

and

$$t_{e\ell} = \left|\frac{\xi+4}{\xi}\right| \frac{M}{\Omega} V_o^{-\frac{\xi}{\xi+4}} \left[2 - e^{-\frac{\xi}{\xi+4}}\right] \tag{22b}$$

The total time of contact $t_{p\ell} + 2\, t_{e\ell}$ is

$$t_c = \left|\frac{\xi+4}{\xi}\right| \frac{M}{\Omega} V_o^{-\frac{\xi}{\xi+4}} \left[3 - e^{-\frac{\xi}{\xi+4}}\right] \qquad (23)$$

The equations derived above are summarized in Table III.

The preceding analysis has yielded expressions for all of the listed impact characteristics in terms of impact velocity. The relationship of this analysis to the Hertz theory as extended by Timoshenko and Goodier and to the analyses of Evans, and Wiederhorn and Lawn can be understood by comparing the exponent of the velocity in equation (23) and the exponent of $\frac{2z}{r_o}$ in equation (4) with the exponents used in the other investigations. The Hertzian case[4,6] is the same as the present analyses if $\xi = 1$ and κ is considered to represent the expression involving the elastic constants in the Hertz theory. The present analysis reduces to that of Wiederhorn and Lawn[7] for damage by sharp indenters when $\xi = 2$ and to that of Evans[6] when ξ is very large. Furthermore the asymmetry of the load history as predicted by Evans[12] in an elastic-plastic impact is described by equation (23) and equation (14).

Table III. Equations for Impact Characteristics

Impact Characteristics	Hertzian Case ($\xi=1$)	Non-Hertzian Case ($\xi\neq1$)
Contact radius	$r_c = r_o\left[\frac{5}{2}\frac{M}{2\kappa\pi r_o^3}\right]^{1/5} V_o^{2/5}$	$r_c = r_o\left[\frac{M}{2}\frac{\xi+4}{\kappa\pi r_o^3}\right]^{1/\xi+4} V_o^{2/\xi+4}$
Radius of indentation	$r_i = 0$	$r_i = r_o\left[\left(\frac{\kappa}{\kappa'}\right)\left(\frac{r_c}{r_o}\right)^{\xi+2}\right]^{1/\xi+2}$
Load	$P = \Omega V_o^{6/5}$	$P = \Omega V_o^{2(\xi+2)/\xi+4}$, $\Omega = \kappa\pi r_o^2\left[\frac{M(\xi+4)}{2\kappa\pi r_o^3}\right]^{\frac{\xi+2}{\xi+4}}$
Time of penetration: time taken by the projectile to go from impact velocity to zero velocity	$t_e = 5\frac{M}{\Omega}V_o^{-1/5}$	$t_p = \left\lvert\frac{\xi+4}{\xi}\right\rvert\frac{M}{\Omega}V_o^{-\xi/\xi+4}$
Depth of damage	$c = \left(\frac{\chi\Omega}{K_{IC}}\right)^{2/3} V_o^{4/5}$	$c = \left(\frac{\chi\Omega}{K_{IC}}\right)^{2/3} V_o^{4/3\frac{\xi+2}{\xi+4}}$
Remaining strength	$\sigma_f = \frac{K_{IC}^{4/3}}{Y(\chi\Omega)^{1/3}V_o^{2/5}}$	$\sigma_f = \frac{K_{IC}^{4/3}}{Y(\chi\Omega)^{1/3}V_o^{\frac{2}{3}\frac{\xi+2}{\xi+4}}}$
Contact time	$t_c = 2t_e$	$t_c = t_p(3-e^{-\xi/\xi+4})$
Coefficient of restitution	$e = 1$ (neglecting stress waves)	$e = \{1-[\left(\frac{\kappa}{\kappa'}\right)\frac{\xi+4}{\xi'+2}\left[\frac{M(\xi+4)}{2\kappa\pi r_o^3}\right]^{\frac{\xi-\xi'}{\xi'+2}} V_o^{\frac{2(\xi-\xi')}{\xi'+2}}]\}^{1/2}$

III. EXPERIMENTAL EVALUATION

The theoretical predictions were compared with experiments using three material combinations; transformation toughened zirconia (TT-ZrO_2) plates* impacted by tungsten carbide spheres (radius 0.795 mm), zinc sulfide plates** impacted by glass spheres (radius 1.5 mm) and glass plates*** impacted by glass spheres (radius 1.5 mm). TT-ZrO_2 and zinc sulfide show elastic-plastic responses whereas the response of the glass is elastic, providing a basis for comparison of these two cases.

Impact on TT-ZrO_2 plates

The contact parameters for the tungsten carbide spheres against TT-ZrO_2 plates were determined by "static" loading with the following results

$$\kappa = 28.5 \text{ GNm}^{-2} \quad \xi = 1.06$$
$$\kappa' = 22 \text{ GNm}^{-2} \quad \xi' = 0.52$$

so that substitution in equation (21) yields

$$e^2 = 9.87 \cdot 10^{-2} V^{0.43}$$

The impact damage was characterized previously.[10] The above equation is compared with the experimental data by Kirchner et al[10] in Figure 2. There is a reasonable agreement between the two curves but the theory predicts higher values of e than were observed by experiment. As indicated in the

---

*TT-ZrO_2 plates in the as-fired condition were supplied by R. C. Garvie of CSIRO.

**ZnS supplied by Raytheon Co., Waltham, Mass.

***Plate glass from Centre Glass, State College, Pa.

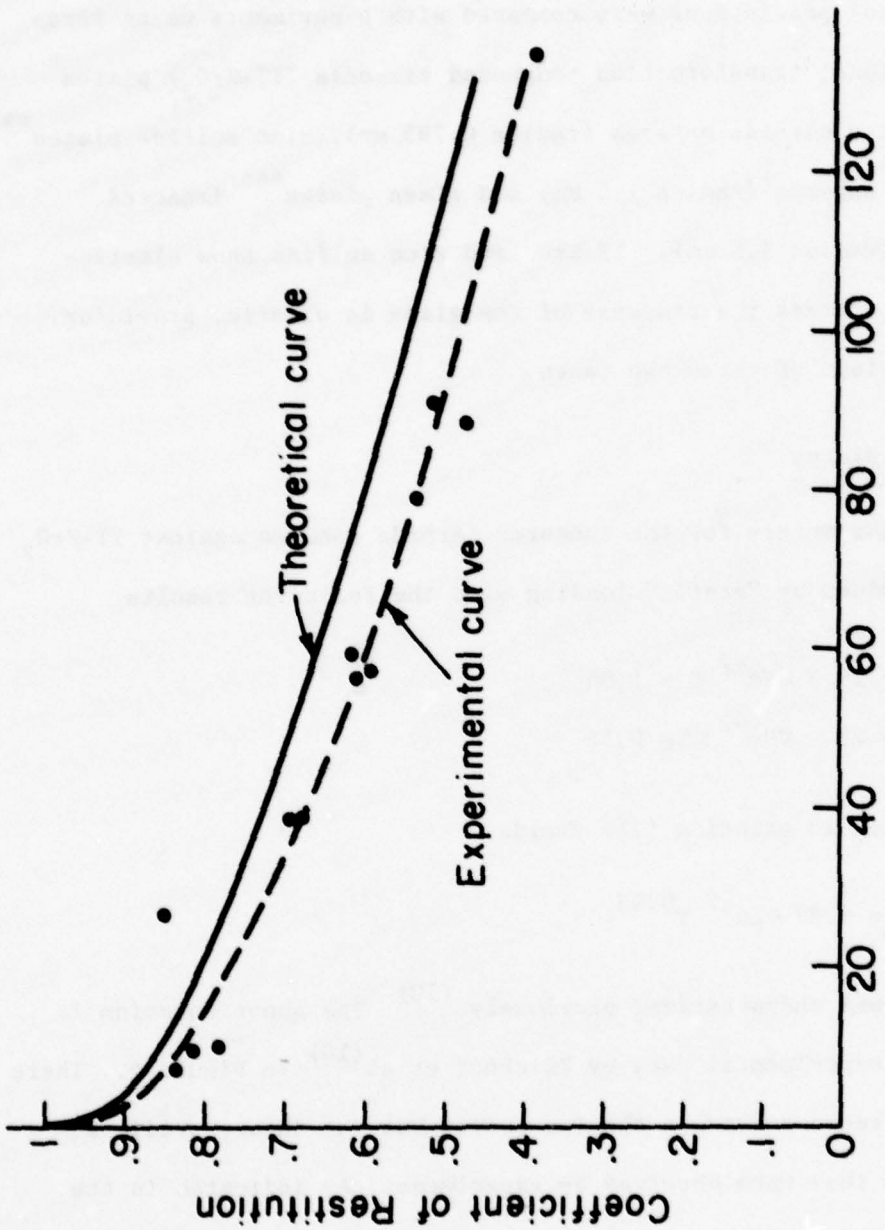


Fig. 2 Coefficient of restitution vs impact velocity for TT-ZrO_2 (as fired) impacted by tungsten carbide sphere.

derivation, the theory does not account for stress wave energy losses. Therefore, one would expect the theoretical rebounding velocities to be higher than those measured experimentally which is consistent with the observations.

Comparisons were also made for the depth of damage and remaining strength as shown in Figures 3 and 4. These comparisons depend on the values of χ, Y and K_{IC} all of which are subject to some uncertainty. Despite this fact, there is reasonable agreement between theory and experiment. It should be noted that, as indicated in Figure 9, the theory does not provide for the threshold velocity necessary to induce the radial cracks but does provide a good estimate of the slope of the crack length vs. impact velocity curve. The sudden change of slope of the experimental curve above $70\,m\cdot s^{-1}$ in Figure 3 is probably a real effect because it was also observed in the under-aged zirconia at somewhat higher velocities. At present, no explanation of this anomaly is available.

There is good agreement between the theoretical and experimental values of remaining strength of as fired TT-ZrO_2 (Figure 4). Based on higher K_{IC} values, the theoretical curves for under-aged and peak-aged TT-ZrO_2 would be expected to yield higher values of remaining strength than the as-fired material. However, κ and ξ have not yet been determined for these materials so the theoretical curves are not available.

As mentioned above, neglect of the stress wave energy in the theory leads to higher values of e, but it also leads to predictions of the load, depth of damage and strength degradation that are too high. The comparisons in Figures 3 and 4 are consistent with these expectations.

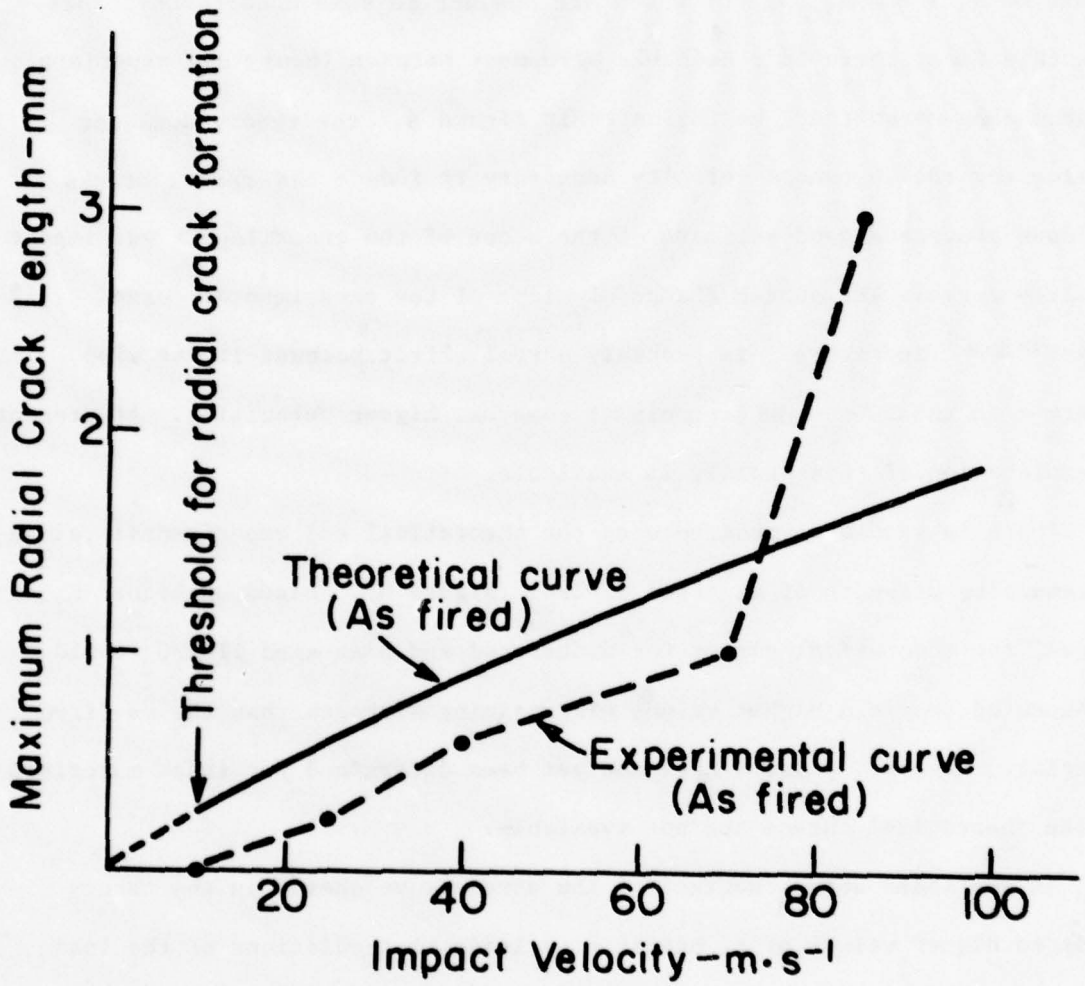


Fig. 3 Maximum radial crack length vs impact velocity for TT-ZrO_2 (as fired) impacted by tungsten carbide sphere.

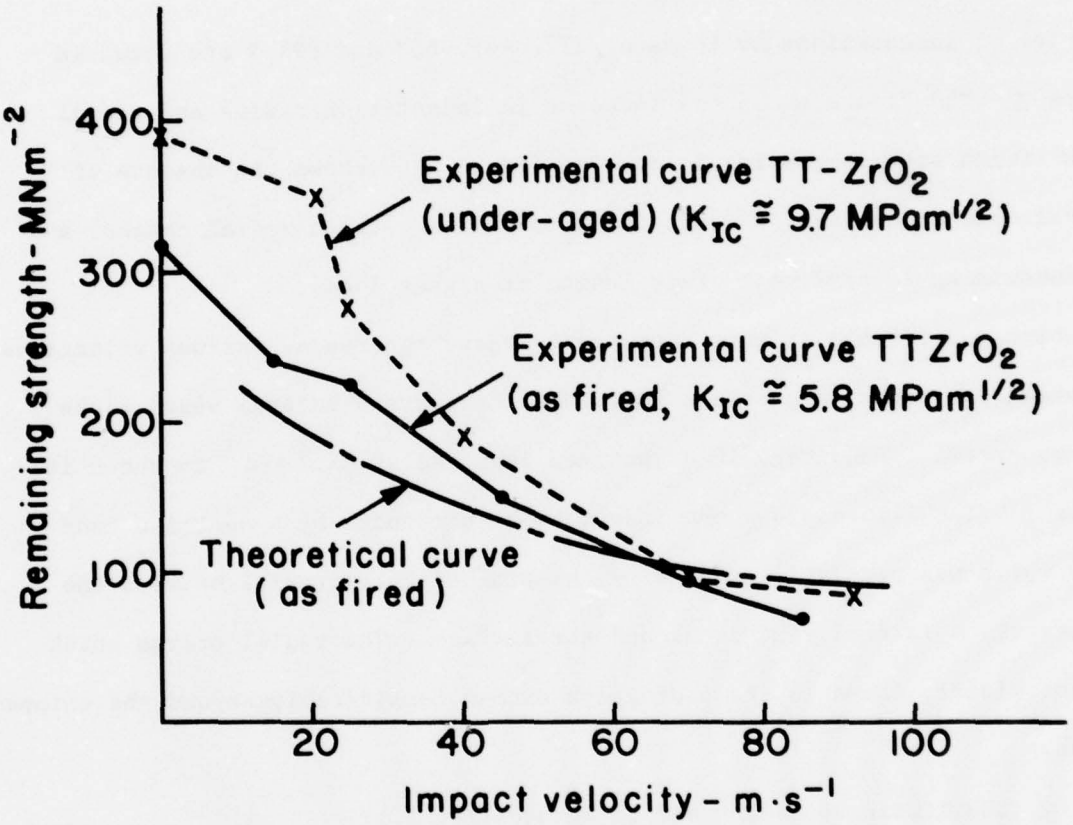


Fig. 4. Remaining strength vs. impact velocity for TT-ZrO_2, as fired and under-aged, impacted by tungsten carbide sphere.

Impact on zinc sulfide plates

The contact parameters for the glass spheres against zinc sulfide plates were determined by static loading with the following results:

$$\kappa = 5.5 \text{ GN m}^{-2} \qquad \xi = 0.78$$

$$\kappa' = 5.5 \text{ GN m}^{-2} \qquad \xi' = 0.27$$

A series of indentations at loads of 222, 445, 668 and 891 N are shown in Figure 5. The figure shows the increase in indentation radius and radial crack length with increasing load. The figure also shows the absence of lateral vent cracks at low loads (no shaded area between radial cracks) and the increasing lateral vent crack length at higher loads.

Zinc sulfide plates were impacted by glass spheres at various velocities. Indentations, Hertzian cone cracks, radial cracks and lateral vent cracks were observed. The damage in a specimen impacted at $68.7 \text{ m} \cdot \text{s}^{-1}$ is shown in Figure 6. The figure shows the indentation surrounded by a Hertzian cone crack which was partially exposed by chipping of the material between the cone crack, a lateral vent crack and the surface. The radial cracks which are not clearly shown in the photograph extend considerably beyond the chipped region.

By substituting κ, κ', ξ and ξ' in equation (21)

$$e = [1 - 4.84 \cdot 10^{-2} V^{0.45}]^{\frac{1}{2}}$$

This equation is compared with experimental impact data in Figure 7. Again, as in the case of TT-ZrO_2, the experimental curve falls below the theoretical curve at least partly because the stress wave energy losses are neglected in the theory.

The radial cracks were assumed to be the strength controlling flaws. The maximum radial crack length was taken, in each case, as the distance from



Fig. 5. Indentations in zinc sulfide caused by a spherical glass indenter (1.5mm radius) at various loads (14X).



Fig.6. Impact damage in zinc sulfide impacted at 68.7 $m \cdot s^{-1}$ by glass sphere, 1.5mm radius (14X).

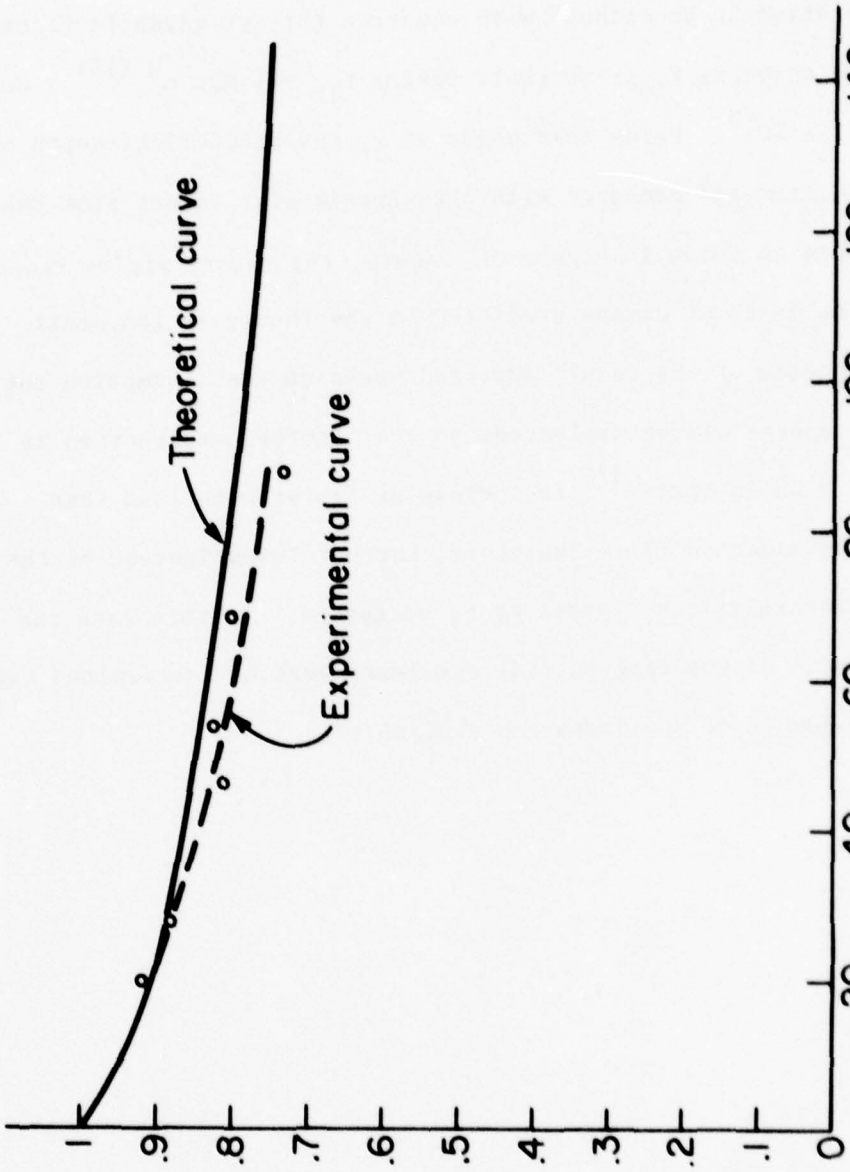


Fig. 7 Theoretical and experimental coefficients of restitution vs impact velocity for ZnS plate impacted by glass spheres (1.5 mm radius).

the edge of the indentation to the tip of the crack. The results for the static tests, plotted in accordance with equation (8) are given in Figure 8. The slope of the curve is K_{IC}/χ so that, taking K_{IC} = 1 MPa $m^{\frac{1}{2}}$, [13] χ was found to be $54.7 \cdot 10^{-3}$. Using this value of χ, the theoretical depth of damage was calculated and compared with the experimental values from the impact experiments as shown in Figure 9. Again, the theory yields reasonable predictions. The depth of damage predicted by the theory is too small which is the opposite of the result expected based on the assumption that the stress wave energy can be neglected, so that another explanation is needed. Figure 8 shows that $c^{3/2}$ is increasing faster with load than expected based on equation (9). Therefore, further investigation of the fracture mechanics relations appears to be necessary. In this case the remaining strengths of the zinc sulfide specimens were not determined because an insufficient number of specimens was available.

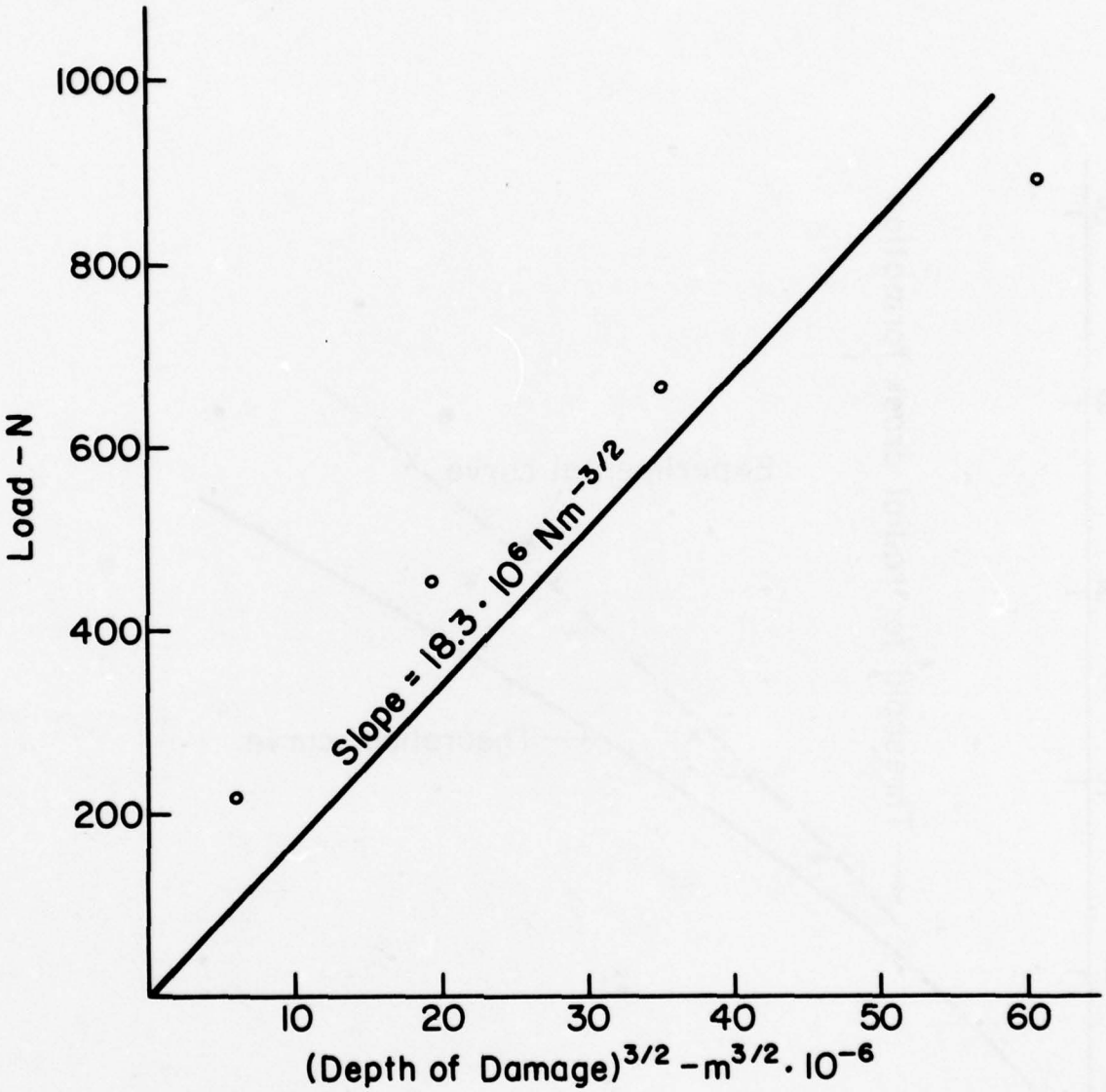


Fig. 8 Load vs (Depth of Damage)$^{3/2}$ for quasi static indentation of a ZnS plate by a glass sphere (3 mm diameter).

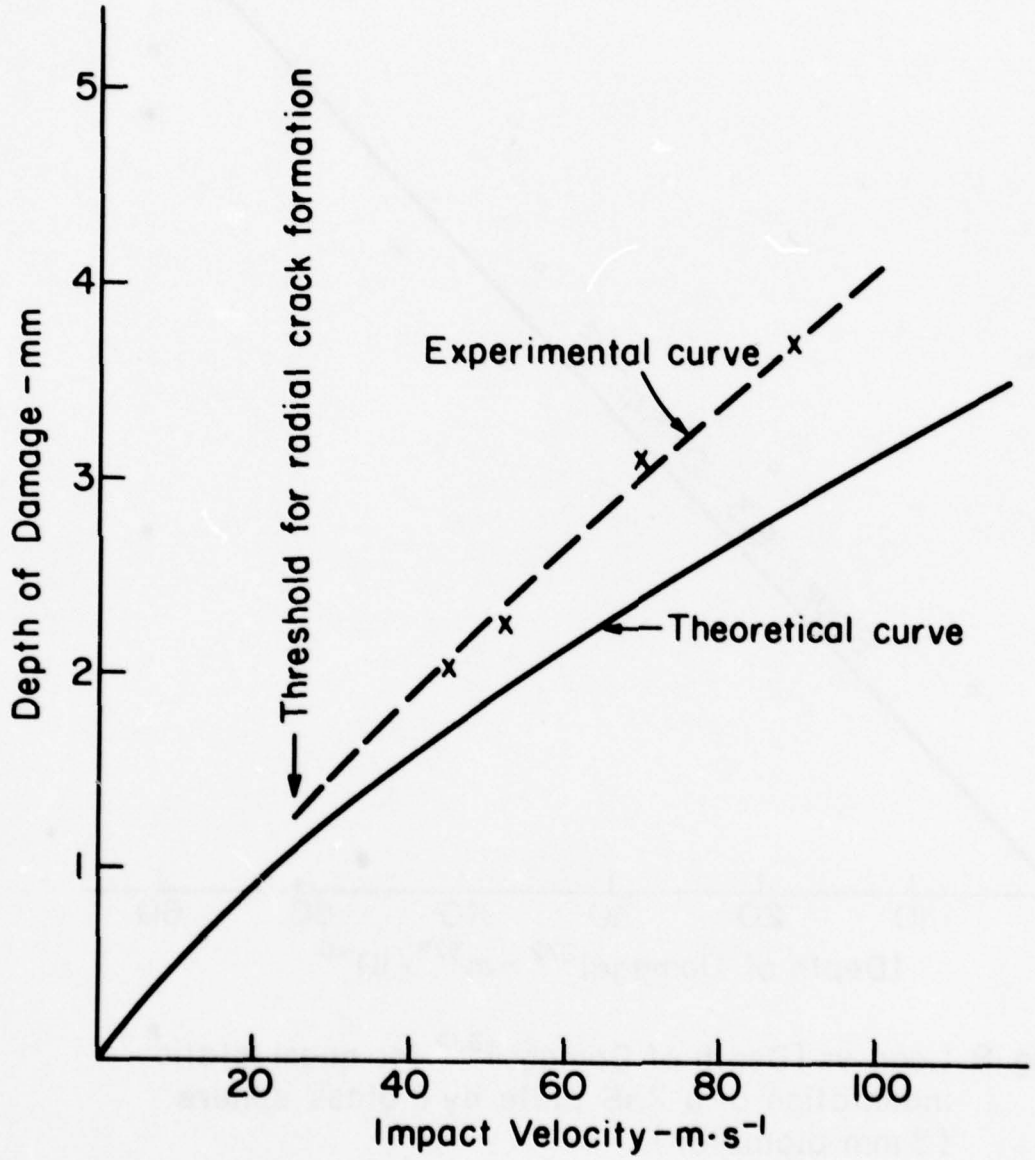


Fig. 9 Depth of damage vs impact velocity for impact of glass sphere (3 mm diameter) on ZnS plate.

Impact on glass plates

The contact parameters for glass spheres against glass plates were determined by static loading with the following results:

$$\kappa = 46.9 \text{ GNm}^{-2} \quad \xi = 2.04$$

Glass spheres do not cause permanent indentations in the glass plates so κ' and ξ' were not determined. It should be pointed out that, whereas the theory assumes a rigid sphere, the contact between glass spheres and plates is an elastic contact between materials having approximately equal values of Young's modulus. Therefore, the elastic deformations in the two bodies are approximately equal leading to a greater contact radius, less penetration and lower pressures than one would expect for a rigid sphere. Despite their apparent simplicity, these contacts between glass spheres and glass plates are far from ideal in terms of the theory.

In the previous cases the evaluation of the theory was introduced by comparing theoretical and experimental values of the coefficient of restitution e. In the case of glass there is no indentation and stress waves are neglected so the theory predicts e = 1. However, e for impacts of glass spheres on glass plates is ~ 0.94 at 20 $\text{m}\cdot\text{s}^{-1}$ and decreases very slowly with increasing velocity until crushing occurs at velocities > 100 $\text{m}\cdot\text{s}^{-1}$.(14)

The theoretical contact radii are compared in Figure 10 with another theoretical curve based on the Hertz theory and with experimental data. The experimental data fall near the theoretical curves but appear to have a lower slope. The effect of neglecting the stress wave energy would be expected to have a weak effect on r_c because r_c varies as the cube root of the load. However, the stress wave energy increases strongly with velocity so that this effect may account for at least part of the lower slope of the experimental data.

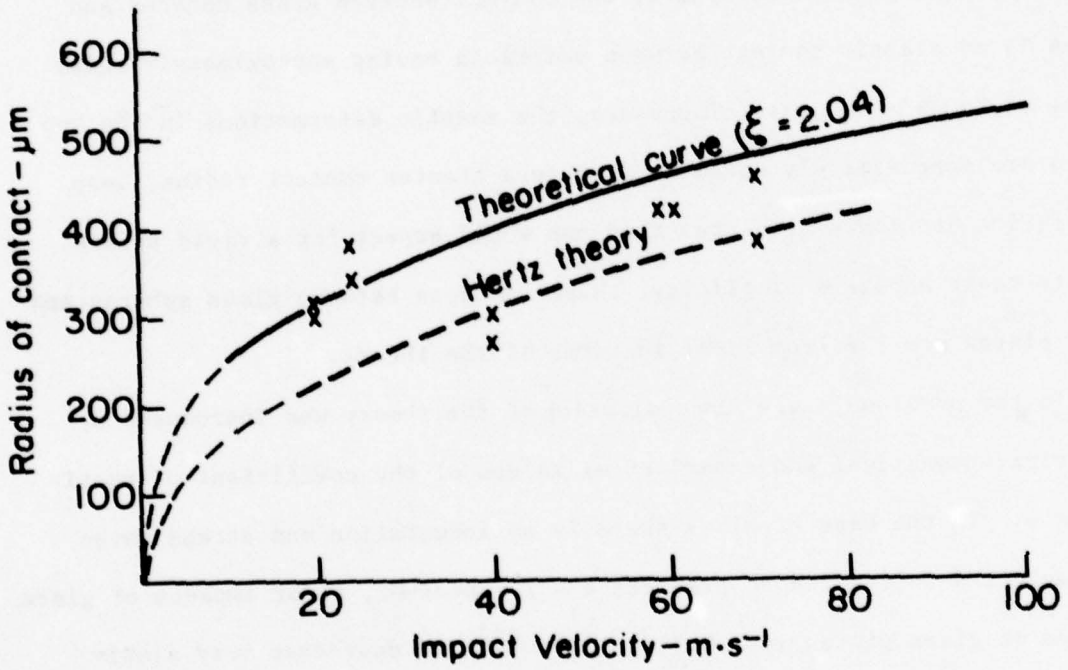


Fig. 10 Radius of contact vs impact velocity, theoretical curve and data points from impact glass on glass[14].

The variation of the load with the impact velocity was compared with theoretical predictions based on the present theory and the Hertz theory. The agreement is reasonable but the experimental data are very scattered because the loads were calculated from the Hertz theory in which the $P \propto r_c^3$ so that errors in measurement of r_c have a large effect on P. For this purpose a direct method of measuring the load is highly desirable.

The variation of the depth of damage with impact velocity was investigated. At low impact velocities the contact radii and the depths of damage were of approximately equal magnitude. Equation (9) for the depth of damage is based on the assumption that the crack is large compared with the contact radius so that the details of the load application do not affect the stress distribution near the crack tip. The data show that the cracks do not become sufficiently large until impact velocities in excess of 60 $m \cdot s^{-1}$ are reached.[14] At higher velocities, a plot of log c vs. log V_o appears to be approximately a straight line but the slope is much greater than that expected based on the present theory or the Hertz theory. The range of available data at these higher velocities is very limited because crushing occurs with a decrease in c at velocities over about 115 $m \cdot s^{-1}$.

The above results show that except for the r_c vs. V_o relationship substantial experimental difficulties have so far prevented a satisfactory comparison of the present theory with experiment for the case of impacts of glass spheres on glass plates.

IV. DISCUSSION

The following discussion deals mainly with qualitative evaluation of the effect of variations in the contact parameters and impact conditions.

Significance of κ, κ', ξ and ξ'.

The significance of κ, κ', ξ and ξ' varies somewhat depending on the nature of the deformation at the impact site. The definition of κ (equation 2) indicates that κ is the pressure existing when the contact radius equals the sphere radius. If the deformation is elastic, κ accounts for the role of the elastic constants in the deformation. For example, if a sphere is pressed into a plate having the same elastic constants the contact radius based on the Hertz theory is[4]

$$r_c = 1.1\left(\frac{P\, r_o}{E}\right)^{1/3} \tag{24}$$

Substituting in equation (2) assuming $P = \pi\, r_c^2\, \eta$ yields

$$\kappa = \eta^{1-\xi}\left(\frac{E}{1.3\pi}\right)^{\xi} \tag{25}$$

Thus, if $\xi = 1$ as one expects for the Hertzian case, then

$$\kappa = \frac{E}{1.3\pi} \tag{26}$$

The experimental results, assembled in Table IV, indicate somewhat higher values of κ and ξ for the elastic contact (glass-glass) than one would expect based on the Hertzian analysis.

TABLE IV

Comparison of Values of κ and ξ for Various Material Combinations

Target Material	Projectile Material	Indenter Radius, r_o μm	κ GNm^{-2}	ξ	Comments
Glass	Glass	1500	46.7	2.04	Elastic contact
ZrO_2 (As Fired)	WC	795	28.5	1.06	Plastic flow in ZrO_2
ZnS	Glass	1500	5.5	0.78	Plastic flow in ZnS

For the cases in which there is plastic deformation of the target or projectile, κ and κ' are related in some way to the hardness of the softer of the contacting materials. ξ and ξ' take care of the increase in the rate of increase of the pressure as the r/r_o ratio increases. In materials that deform plastically, this variation may be caused, in part, by work hardening.

The constants κ, κ', ξ and ξ' are difficult to measure. The range of pressures covered by the measurements is much smaller than desired. At low pressures the scatter in the results is large because of experimental errors. At higher pressures the measurements are likely to be terminated by crushing of the sphere. Greater weight should be given to the measurements at higher pressures in determining the slopes (ξ and ξ'). However, at best, the present techniques yield only rough estimates.

Stress Wave Energy

Stress wave energy can be expected to have a significant role in impact phenomena. In elastic impacts (for example, glass-glass) the stress wave energy is the dominant loss mechanism and for firmly supported targets it is the principal factor determining the coefficient of restitution[15]. Hunter[16] gave the following expression for the stress wave energy in a target as a function of velocity.

$$W_s = \tfrac{1}{5} MV^2 \hat{\lambda} V^{3/5} \tag{27}$$

where

$$\hat{\lambda} = \frac{2 \tau M^{-1/5} r_o^{3/5} g^{-6/5}}{\rho c_o^3} \tag{28}$$

and

$$g = \left[\frac{1-\sigma^2}{E} + \frac{1-\sigma_1^2}{E_1}\right] \tag{29}$$

in which σ is the Poisson's ratio and the lack of a subscript signifies the target and the subscript 1 signifies the projectile and

$$\tau = (1.068)^5(1+\sigma)\left(\frac{1-\sigma}{1-2\sigma}\right)^{\frac{1}{2}}\left(\frac{16}{15}\right)^{6/5} J\left\{\int_0^\infty \frac{(\zeta^2-1)^{\frac{1}{2}}\zeta d\zeta}{F_o(\zeta)}\right\} \qquad (30)$$

where J indicates the imaginary part of the complex variable. The details of the derivations are given by Hunter[16]. However in our case an additional term should be added to the equation to account for the stress wave energy in the projectile.

For a rigid sphere, a derivation similar to that for a half space can be done. According to Love[17], a half space and a sphere are one and the same thing mathematically speaking. They are geometrically inverse of each other. Indeed, taking the derivation of Miller and Pursey[18,19] for a half space and modifying it by applying the boundary conditions for a sphere, introduces new terms in the differential equations (37-40) in reference 14. These new terms, due to application of Hankel's transform to the equations of elasticity[20-23], are dependent upon the displacement and distortion of the surface of the sphere, as well as their derivatives in regard to the radial direction of cylindrical coordinates centered at the impact site with an axis perpendicular to the surface. With the assumption of a rigid sphere, these additional terms will vanish and the solutions given by Miller and Pursey[18,19] and by Hunter[16] for a half space will be valid for a projectile. Hence, the total stress wave energy absorbed during impact can be written as

$$W_s = \lambda\ (\tfrac{1}{2} MV_o^{\frac{1}{2}})\ V^{3/5} \qquad (31)$$

in which $$\lambda = \hat{\lambda}\ (1 + \frac{\rho c_o}{\rho_1 c_{o_1}}) \tag{32}$$

with the impedance ratio, $\frac{\rho c_o}{\rho_1 c_{o_1}}$, taking account of the distribution of energy between the target and the projectile. This stress wave energy will enter on the right side of equation (5).

$$\tfrac{1}{2}\, MV_o^2 = \frac{\kappa\, \pi\, r_o^3}{\xi+4}\, (\frac{r}{r_o})^{\xi+4} + \tfrac{1}{2}\, MV_o^2\, \lambda\, V_o^{3/5} \tag{33}$$

In the relationships previously derived (Table II) the term V_o will thus be replaced by $V_c(1-\lambda V_o^{3/5})^{\frac{1}{2}}$. Because of absorption of energy by the stress waves, the radius of contact, load and depth of damage will be smaller than indicated by equations (6,8,10) while the remaining strength and contact time are greater than expected based on equations (12) and (23). The coefficient of restitution will be smaller than expected.

Sharp Indenter

For a sharp indenter, a similar derivation can be done in which

$$\eta = \kappa(\frac{r}{z_o})^{\xi} \tag{34}$$

or $$\eta = \kappa(\frac{a}{b})^{\xi} \tag{35}$$

where z_o is the height of the indenter for a conical indenter and a and b are the diagonals of a pyramid at the contact and at the base as shown in Figure 11.* Thus, the equations in Table III can be adapted for the appropriate sharp indenter by substituting the symbols as shown below:

---

*This case is similar to the Ludvick or Vicker's hardness[9].

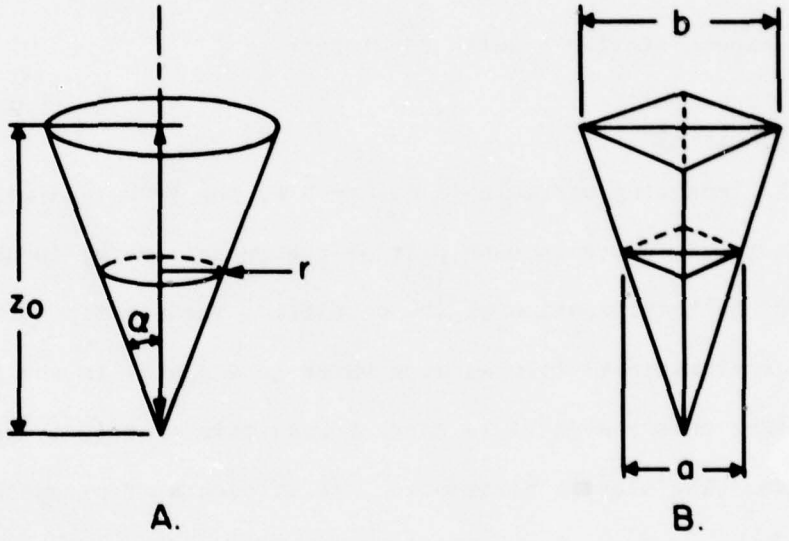


Fig. II. A. Conical indenter. B. Pyramidal regular indenter with their geometrical characteristics.

	Sphere	Cone	Pyramid
Contact Parameter	r	r	a
Normalizing Parameter	r_o	z_o	b

Sharp indenters are expected to increase the depth of damage compared with that of blunt indenters. Hence, the strength will be lower. Such results have been observed for static indentations[24], and grinding[25,26] and one would expect similar results for impact.

Deformable particle

If the impacting particle is deformable, the peak load will be lower than for a rigid sphere because part of the impact energy is absorbed by the work of bulk deformation of the particle. The elastic deformation will induce vibrations (like bending waves in a plate) in the particle and, to the extent that the particle carries away this energy, it is an impact energy loss. The plastic deformation, if it occurs, represents another energy loss mechanism. Consequently, assumption of a rigid projectile overestimates the maximum load, the depth of damage and the strength degradation.

Impact at an angle

For impacts at an angle on brittle materials, one can assume that the impact damage is controlled by the vertical component of velocity. Therefore, compared with perpendicular impact, impact at an angle leads to lower loads, depth of damage and strength degradation. In their analysis of erosion, B. J. Hockey et al[27] made similar assumptions.

V. SUMMARY AND CONCLUSIONS

A comprehensive theory of elastic-plastic impact was derived. The theory was evaluated by experiments involving impacts of tungsten carbide spheres on TT-ZrO_2, glass spheres on zinc sulfide and glass spheres on glass. Agreement with the theory was reasonable for elastic-plastic impacts on TT-ZrO_2 and zinc sulfide but for elastic impacts on glass experimental and theoretical problems were encountered that require further investigation.

Approaches by which the theory can be extended to take stress waves, sharp particles, deformable particles, and impact at an angle into account, were described.

REFERENCES

1. Hertz, H. "On the Contact of Elastic Solids", from Miscellaneous Papers, MacMillan and Co. Ltd., London (1896) p. 146.

2. Evans, A. G., "Strength Degradation by Projectile Impacts", J. Amer. Ceram. Soc. 56(8) 405-409 (1973).

3. Evans, A. G. and R. Wilshaw, "Particle Damage in Brittle Solids; I, Observations, Analysis, Implications", Acta Met. 24, 939-958 (1976).

4. Timoshenko, S. and J. N. Goodier, "Theory of Elasticity", McGraw-Hill, New York (1951).

5. Pao, Yoh-Han, "Extension of the Hertz Theory of Impact to the Visco-elastic Case", J. Appl. Phys. 26(9) 1083-1088 (1955).

6. Evans, A. G., "Impact Damage in Ceramics", from Fracture Mechanics of Ceramics, Vol. 3, Edited by R. C. Bradt, D. P. H. Hasselman and F. F. Lange, Plenum, New York (1978) pages 303-331.

7. Wiederhorn, S. M. and B. R. Lawn, "Strength Degradation of Glass Impacted with Sharp Particles: I. Annealed Surfaces", Submitted to J. Amer. Ceram. Soc.

8. O'Neil, H., "Hardness Measurement of Metals and Alloys", Chapman and Hall, Ltd., London (1967).

9. Tabor, D. "The Hardness of Metals", The Clarendon Press, Oxford (1951).

10. Kirchner, H. P., R. C. Garvie, R. M. Gruver and D. M. Richard, "Localized Impact Damage in Transformation Toughened Zirconia", To be published in Mater. Sci. Eng.

11. Lawn, B. R. and D. B. Marshall, "Contact Fracture Resistance of Physically and Chemically Tempered Glass Plates: A Theoretical Model", Phys. Chem. Glasses 18(1) 7-18 (1977).

12. Evans, A. G. and T. R. Wilshaw, "Dynamic Solid Particle Damage in Brittle, Materials: An Appraisal" J. Mater. Sci. 12, 97-116 (1977).

13. Evans, A. G., T. R. Wilshaw, J. C. Chesnutt and H. Nadler, "Quasi-Static Solid Particle Damage in Brittle Materials", Rockwell International Science Center First Report SC5023.3TR, Contract N00014-75-C-0669 (February, 1976).

14. Kirchner, H. P. and R. M. Gruver, "Localized Impact Damage in Glass", Mater. Sci. Eng. 28, 153-160 (1977).

15. Kirchner, H. P. and R. M. Gruver, "The Effect of Localized Impact Damage on Energy Losses During Impact", Mater. Sci. Eng. 33, 101-106 (1978).

16. Hunter, S. C., "Energy Absorbed by Elastic Waves During Impact", J. Mech. Phys. Solids 5, 162-171 (1957).

17. Love, A. E. H., "Mathematical Theory of Elasticity", Cambridge University Press, Cambridge (1920).

18. Miller, G. F. and H. Pursey, "The Field and Radiation Impedance of a Mechanical Radiator on the Free Surface of a Semi-Infinite Isotropic Solid", Proc. Roy. Soc. A 223, 521-541 (1954).

19. Miller, G. F. and H. Pursey, "On the Partition of Energy Between Elastic Waves in a Semi-Infinite Solid", Proc. Roy. Soc. A233, 55-69, (1955).

20. Mills, John, "Integral Transforms in Applied Mathematics," Cambridge University Press, Cambridge (1971).

21. Columbo, S., "La Transformation de Mellin et de Hankel, Application à la Physique Mathématique", Centre National de la Recherche Scientifique, Paris (1959).

22. Watson, G. N., "A Treatise on the Theory of Bessel Functions", Cambridge University Press, Cambridge (1922).

23. Jeffreys, H. and B. S. Jeffrey, "Methods of Mathematical Physics", Cambridge University Press, Cambridge (1950).

24. Lawn, B. R., E. R. Fuller and S. M. Wiederhorn, "Strength Degradation of Brittle Surfaces: Sharp Indenters", National Bureau of Standards Report NBSIR 75-661, (May, 1975).

25. Kirchner, H. P., R. M. Gruver and D. M. Richard, "Fragment Formation and Damage Fenetration During Machining of Ceramics", Ceramic Finishing Company Summary Report, Contract NSF-C-APR77-19818 (March, 1978).

26. Kirchner, H. P., R. M. Gruver and D. M. Richard, "Fragment Formation and Damage Penetration During Machining of Ceramics", Presented at the Second Symposium on Ceramic Machining and Surface Finishing, National Bureau of Standards, Nov. 13, 1978, To be published in the proceedings.

27. Hockey, B. J., S. M. Wiederhorn and H. Johnson, "Erosion of Brittle Materials by Solid Particle Impact", from Fracture Mechanics of Ceramics, Vol. 3, Edited by R. C. Bradt, D. P. H. Hasselman and F. F. Lange, Plenum, New York (1978) p. 379-402.

Localized Impact Damage in Transformation Toughened Zirconia

by

H. P. Kirchner*
R. C. Garvie**
R. M. Gruver*
D. M. Richard*

*Ceramic Finishing Co., State College, PA., U.S.A.
**CSIRO, Division of Materials Science, Melbourne, Australia.

Acknowledgements

At CSIRO we thank R. R. Hughan, V. Gross and C. Urbani for the preparation of specimens. At Ceramic Finishing Co. we are pleased to acknowledge the contributions of our associates and the sponsorship of the office of Naval Research.

Abstract

Zirconia specimens, partially stabilized with calcia and aged for various times to vary K_{IC}, were impacted by glass, steel and tungsten carbide spheres. The impact damage was characterized. The zirconia was resistant to damage by the softer spheres, glass and steel, but the tungsten carbide caused visible damage (indentations) at impact velocities as low as 9 ms^{-1}. At higher velocities, radial, lateral vent, and circumferential cracks were observed. Indentation and stress wave energy loss mechanisms account for most of the observed energy losses. The remaining strengths after impact increased somewhat less than expected with increasing K_{IC}.

I. Introduction

The fracture toughness of zirconia can be increased by proper control of composition and heat treatment[1-3]. Calcia partially stabilized zirconia was used in this investigation. In this material aging at intermediate temperatures, usually in the range 1200-1500°C in the cubic-tetragonal phase field[4], leads to coarsening of the tetragonal precipitate in the much larger cubic crystals. At room temperature, this coarsening increases the susceptibility of the tetragonal phase to transformation to the monoclinic. Tensile stress further encourages this transformation because the monoclinic phase is less dense than the tetragonal phase. Therefore, when cracks propagate through the material, the tensile stress concentrated at the crack tip causes the tetragonal crystals within a few micrometers of the crack to transform to monoclinic[5]. This transformation is believed to be responsible for the high values of critical stress intensity factor (K_{IC}) observed for these materials. Therefore, the material is sometimes termed transformation toughened zirconia (TT ZrO_2).

TT ZrO_2 is unique in that machining (grinding) causes an increase in strength[1,6]. This strength increase is believed to be caused by compressive surface stresses formed by the expansion during transformation to the monoclinic phase which is induced by the grinding. The decision to investigate localized impact damage in TT ZrO_2 was based on the high K_{IC} values and the unique surface effect in these materials which were expected to reduce the impact damage.

II. Procedures

Calcia partially stabilized ZrO_2 with four 1300°C aging treatments (as-fired, 0 hours; underaged, 30 hours; peak-aged, 48 hours; and overaged, 57 hours) was prepared in the form of rectangular bars, 3 x 10 x 40 mm, with ground (50 grit) surfaces. One large surface of each bar was polished with 6 μm and 1 μm diamond compound and either 1/4 μm diamond compound or 1 μm gamma alumina in successive steps on a paper covered rotating lap. At intervals during polishing the relative amounts of monoclinic phase in the surfaces were monitored by x-ray diffraction. Polishing was stopped when the reduction of the monoclinic phase no longer continued. The other surfaces of the bars were left in the machined condition. One reason for doing this was the expectation that the compressive surface stresses due to machining would reduce the probability of fractures originating at the edges.

A preliminary investigation was used to select a suitable sphere material and size for the impact tests. Glass, steel and tungsten carbide spheres were tested and tungsten carbide was chosen for the main impact experiments. In these experiments, ZrO_2 bars with each of the four treatments were impacted on the polished surfaces at various velocities. The impacting and rebounding velocities were measured by measuring the distances traveled by the spheres between flashes of a stroboscope* as indicated by phtographs taken by a camera with its lens open during the flight of the sphere. The coefficient of restitution was calculated as

---

*General Radio Strobotac 1538-A

the ratio of the rebound velocity to the impact velocity. The specimens were coated with a thin layer of soot. The contact radii were measured from the impressions in the soot. The impact damage was characterized. TT ZrO_2 is indented readily by the tungsten carbide spheres. The radii of the indentations were measured. In each specimen the radius of the longest radial crack, if present, was measured as the distance from the center of the indentation to the tip of the crack.

The flexural strengths of the impacted specimens were measured by three point loading on a one inch span to evaluate the strength degradation caused by the impact damage. The fracture surfaces were examined by optical and scanning electron microscopy and the depth of damage (depth of the disturbed area) under the impact site was measured. The critical stress intensity factors (K_{IC}) of the materials were measured by the single edge notched beam (SENB) method[7,8] and estimated from the fracture stresses and the depths of damage or radii of radial cracks.

III. Results and Discussion

Strengths of the materials before impact

A preliminary aging curve was available for specimens of this particular composition aged at 1300°C (Figure 1). These preliminary strengths were determined using bars (1/8 x 1/8 x 1-1/2 in) with 150 grit diamond ground surfaces from which 40 μm was removed on the final pass. The strengths were measured in four-point loading (1.125 in outer span, 0.5 in inner span) at a loading rate that resulted in failure in 1-2 min. This curve was used to select the aging times.

One of the large surfaces of each specimen was polished to provide a smooth surface for observation of the impact damage and to remove the compressive surface stresses caused by grinding so that these stresses would not reduce the extent of damage as has been shown previously for other materials[9,10]. The final step in polishing the first three specimens of each aging treatment used 1 μm gamma alumina in liquid suspension. This process reduced the monoclinic phase in the peak-aged material to about 32% of the amount present in the original ground surfaces. Subsequently, the remainder of the specimens were polished by a process in which 1/4 μm diamond compound was used as the last step. This process reduced the monoclinic phase in the surface to about 10% of the amount originally present. The flexural strengths of three specimens from each of these aging, grinding and polishing treatments were measured and these results are including in Figure 1. The strengths were measured in three point loading on a one inch span with the polished surfaces in tension.

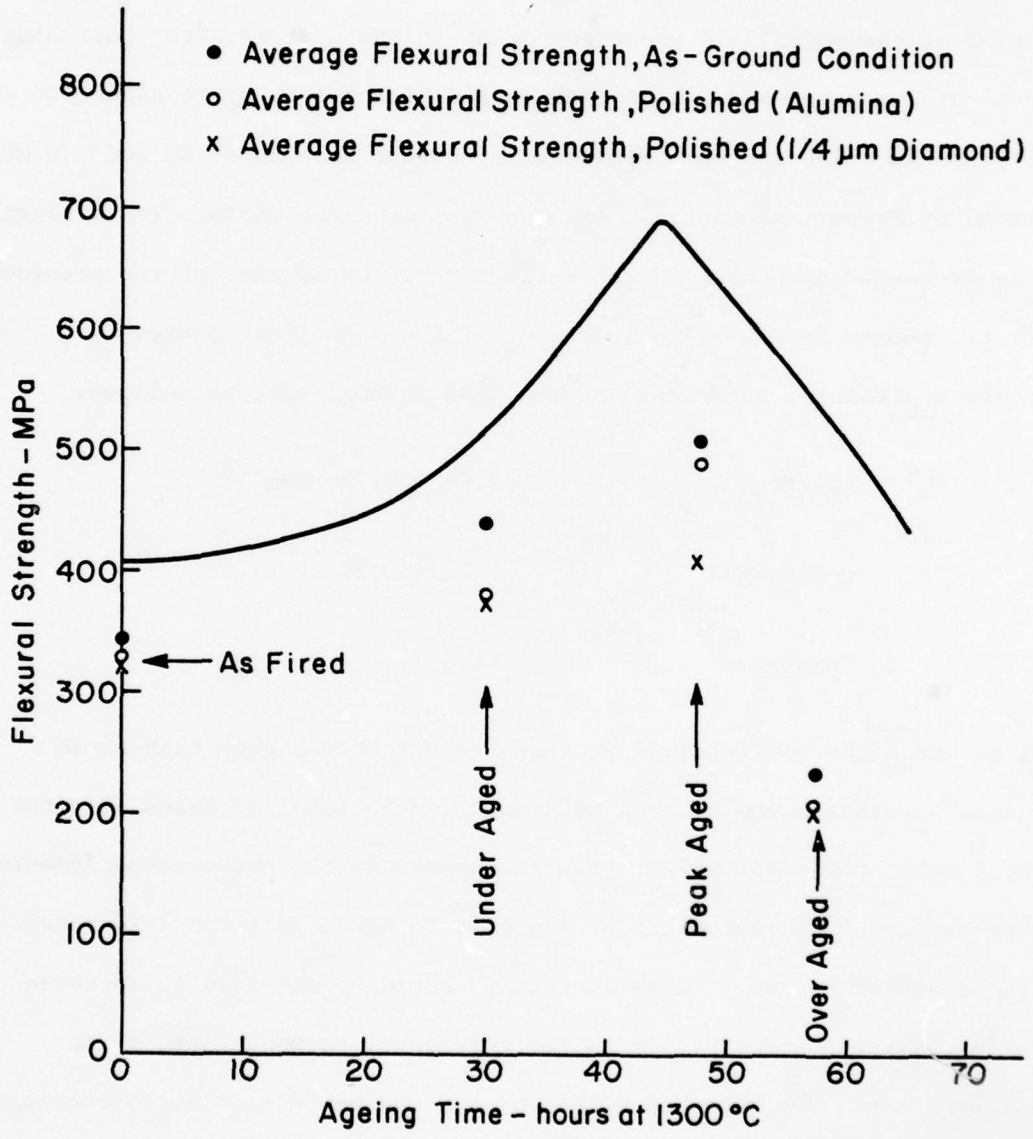


Figure 1 Preliminary Ageing Curve for TT ZrO_2 and Resulting Flexural Strengths of Specimens with Ground or Polished Surfaces

Removal of the ground surface decreased the strength, as expected. The decrease was greater for specimens polished with 1/4 μm diamond than it was for those polished with 1 μm alumina which is consistent with the fraction of the monoclinic phase remaining in the surface after polishing. Removal of the stressed surface reduces the strength by up to about 100 MPa. This decrease can be compared with decreases of about 60 and 120 MPa observed by Pascoe and Garvie[6] in two sets of experiments. The strengths of the over-aged specimens were sometimes very low because of the presence of cracks caused by excessive formation of the monoclinic phase.

The K_{IC} values, determined by the SENB method, were as follows:

As-fired	5.84 ± 0.77 MPam$^{1/2}$
Under-aged	8.71 ± 0.67
Peak-aged	12.99

This method tends to yield values that are slightly higher than those obtained by other methods, even with more conventional ceramics. In the present case, the compressive stresses induced by the phase transformation during sawing of the notch can be expected to cause additional increases in the measured values. These increases should be expected to increase with increasing susceptibility to the tetragonal to monoclinic phase transformation. The measured values of K_{IC} can be reduced by correcting for the effect of the residual surface stress. If it is assumed that the residual stress in the notch is approximately equal to the residual stress originally induced in the surface by grinding and subsequently removed by

polishing, the ratio of the strength in the polished condition to that in the ground condition (Figure 1) can be used to correct the above K_{IC} values with the following results:

As-fired	5.5 $MPam^{1/2}$
Under-aged	7.6
Peak-aged	10.5

These values will be compared with values based on flaw size estimates in a later section.

Preliminary experiments to select impacting spheres

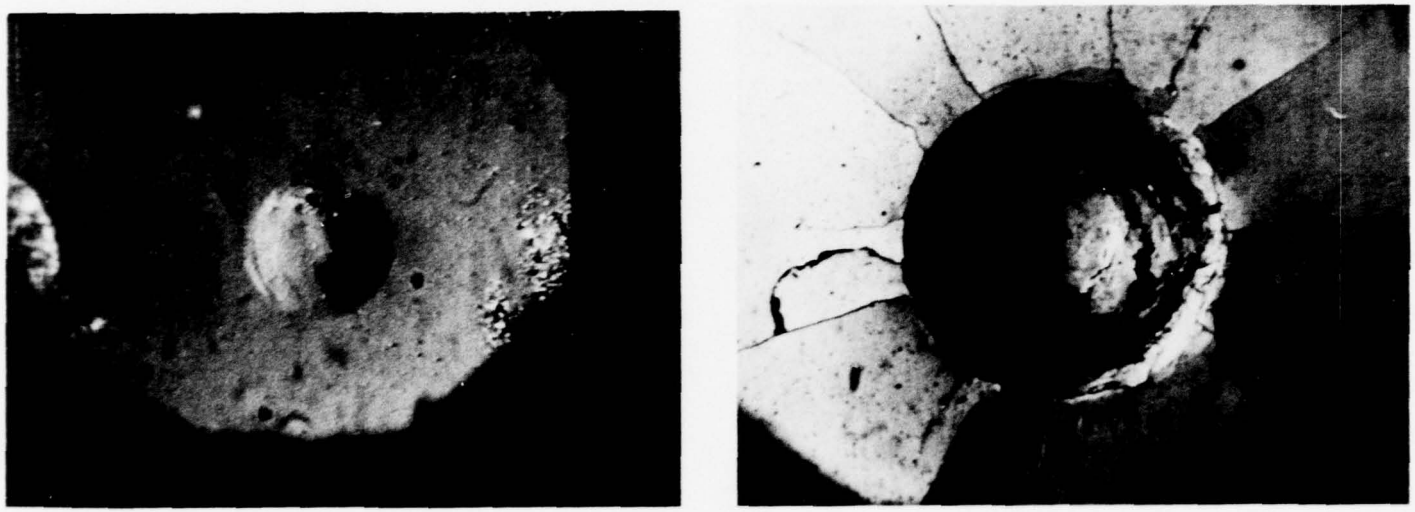
TT ZrO_2 specimens were impacted by glass, steel and tungsten carbide spheres to provide information on which to base the selection of spheres to be used for the principal experiments. Glass spheres (3 mm diam) did not induce visible damage in the surfaces at velocities up to 124 ms^{-1} at which the glass crushed completely. Steel spheres (1.59 mm diam) did not induce visible damage at velocities up to 198 ms^{-1} but the spheres flattened so that the use of higher velocities seemed unpromising. Tungsten carbide spheres (1.59 mm diam) indented the surfaces readily even at low velocities and also caused crack formation. The coefficients of restitution of the three materials were consistent with these observations.

It was clear from these experiments that TT ZrO_2 was very resistant to impacts by the softer projectiles, glass and steel. In many ceramics Hertzian cone cracks, visible as ring cracks in the surfaces, or other visible damage, would have been induced by these spheres. In order to be able to observe and characterize variations in localized impact damage in the available range of velocities, tungsten carbide spheres were selected for the principal impact experiments.

Characterization of impact damage

The types of damage observed at the impact sites included indentations and radial, lateral vent, and circumferential cracks. The impact sites for two impact velocities are shown in Figure 2. At 13.9 ms^{-1} (Figure 2A) the impact damage, at least as observed on the surface, consists of a small, well-formed indentation. Indentations were observed at velocities as low as 9 ms^{-1}. At 71.4 ms^{-1} (Figure 2B) the impact damage, as observed on the surface, consists of an indentation containing circumferential cracks and surrounded by radial cracks. At still higher velocities, lateral vent cracks extend to the surface leading to chipping between the radial cracks.

Observation of indentations at velocities as low as 9 ms^{-1}, means that the yield stress has already been exceeded at this velocity. The stresses were estimated. Static loads were applied to the surfaces using the same spheres as indenters. The contact radii and indentation radii were measured. Then, the impact loads were estimated based on the assumption that the impact and static loads of the same magnitude cause



(a) 13.9 ms^{-1} (b) 71.4 ms^{-1}

Figure 2 Impact Damage in As Fired TT-ZrO_2 Impacted by 1.588 mm. Diameter Tungsten Carbide Spheres (82X)

indentations of the same size. At the lowest loads at which indentations were observed, the average pressure (p_o) on the indentation was about 7 GPa. Gilman[11] has pointed out that the ratio of the hardness to the yield stress increases in nonmetallic crystals depending upon the relative difficulty of flow on the various glide systems. Therefore, it is not possible to calculate a definite value of yield stress from the indentation pressure. According to the Hertzian stress distribution, the radial stress at the circumference of the contact area is 0.166 p_o which corresponds to about 1.2 GPa in this case. This localized stress is about three times the measured flexural strengths of this material. Therefore, it is reasonable to expect flaw growth and circumferential crack formation under the influence of these stresses.

Energy losses during impact

For impacts of tungsten carbide spheres on TT-ZrO_2, the coefficient of restitution decreases approximately linearly with impact velocity as shown in Figure 3. The slope of this curve contrasts strikingly with the slope obtained at room temperature for impacts of glass spheres on glass plates[12] which show only a very slowly decreasing coefficient of restitution. However, the slope is similar to that observed for glass at temperatures above the softening point where substantial indentation occurs because of viscous flow[13]. This similarity is evidence that plastic deformation at the impact site is responsible for much of the observed decrease in the coefficient of restitution. The aging treatments have little effect on the coefficient of restitution.

The kinetic energies of the impacting and rebounding spheres were calculated and used to calculate the kinetic energy losses. These losses

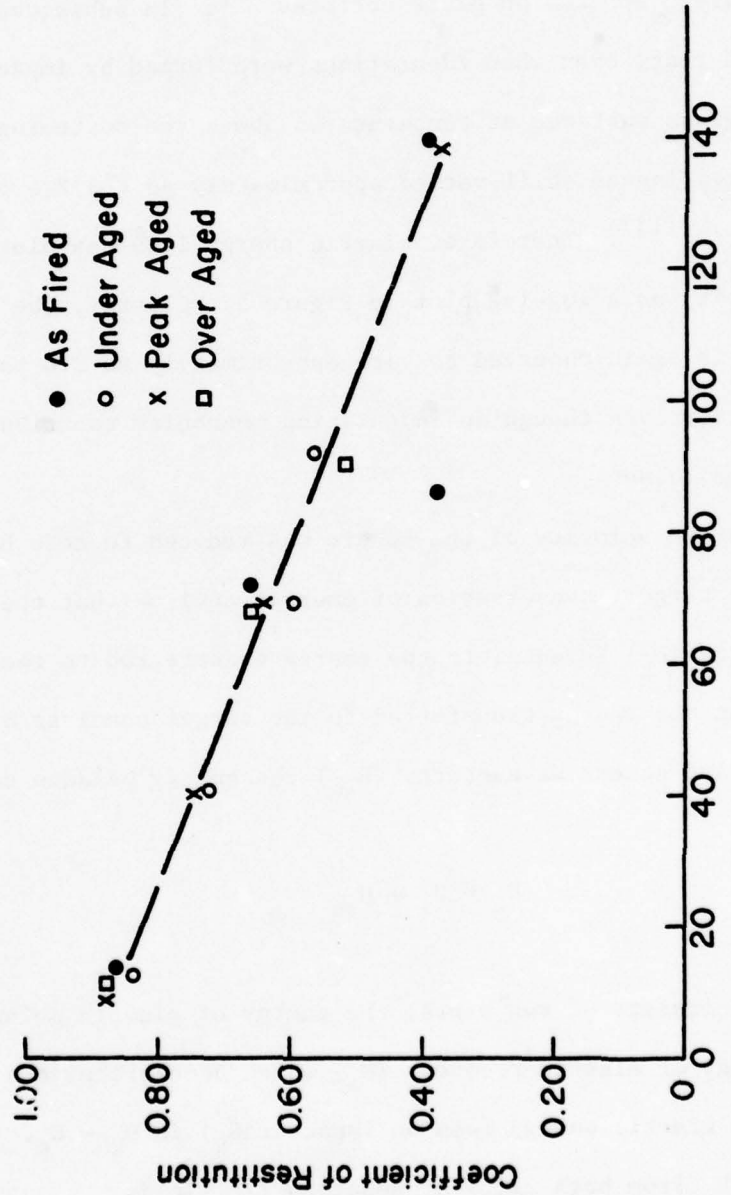


Figure 3 Coefficient of Restitution vs. Impact Velocity for TT ZrO_2 Impacted by 1.588 mm. diam. Tungsten Carbide Spheres

are plotted as the solid line in Figure 4. Hunter[14] found analytically that the stress wave energy induced by elastic impact varied as the 2.6 power of the impact velocity. Evidently, the stress waves account for all or almost all of the energy losses occurring during room temperature impacts of glass spheres on glass surfaces[15]. In subsequent experiments, it was found that, even when identations were formed by impacts of glass spheres on glass surfaces at temperatures above the softening point, the kinetic energy losses still varied approximately as the 2.6 power of the impact velocity[13]. Therefore, kinetic energy loss was plotted vs. the impact velocity on a log-log plot in Figure 5. Clearly, the kinetic energy loss is again observed to vary approximately as 2.6 power of the impact velocity even though an indentation mechanism contributes substantially to the losses.

Because the velocity of the sphere was reduced to zero by impact on a stationary target, conservation of energy requires that the incoming kinetic energy (U_k) is equal to the energy transferred to the target. Assuming that the energy transferred to the target consists of indentation energy (U_i) and stress wave energy (U_{sw}) the energy balance can be written

$$U_k = U_i + U_{sw} \tag{1}$$

However, U_i consists of two parts, the energy of plastic deformation (U_p) and the energy of elastic recovery (U_e) which accelerates the rebounding sphere. The kinetic energy loss on impact (ΔU_k) is $U_k - U_e$. Therefore, subtracting U_e from both sides of Equation (1) yields

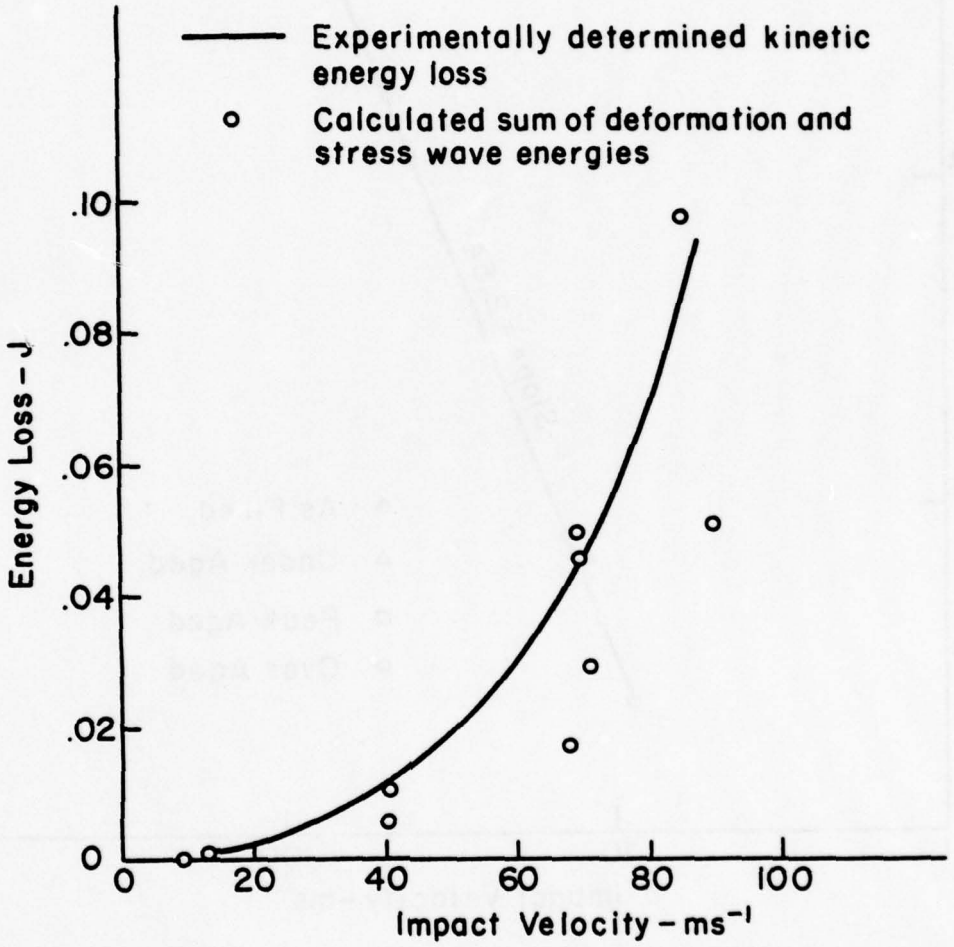


Figure 4 Energy Loss vs. Impact Velocity for TT ZrO_2 Impacted by 1.588mm. Diameter Tungsten Carbide Spheres

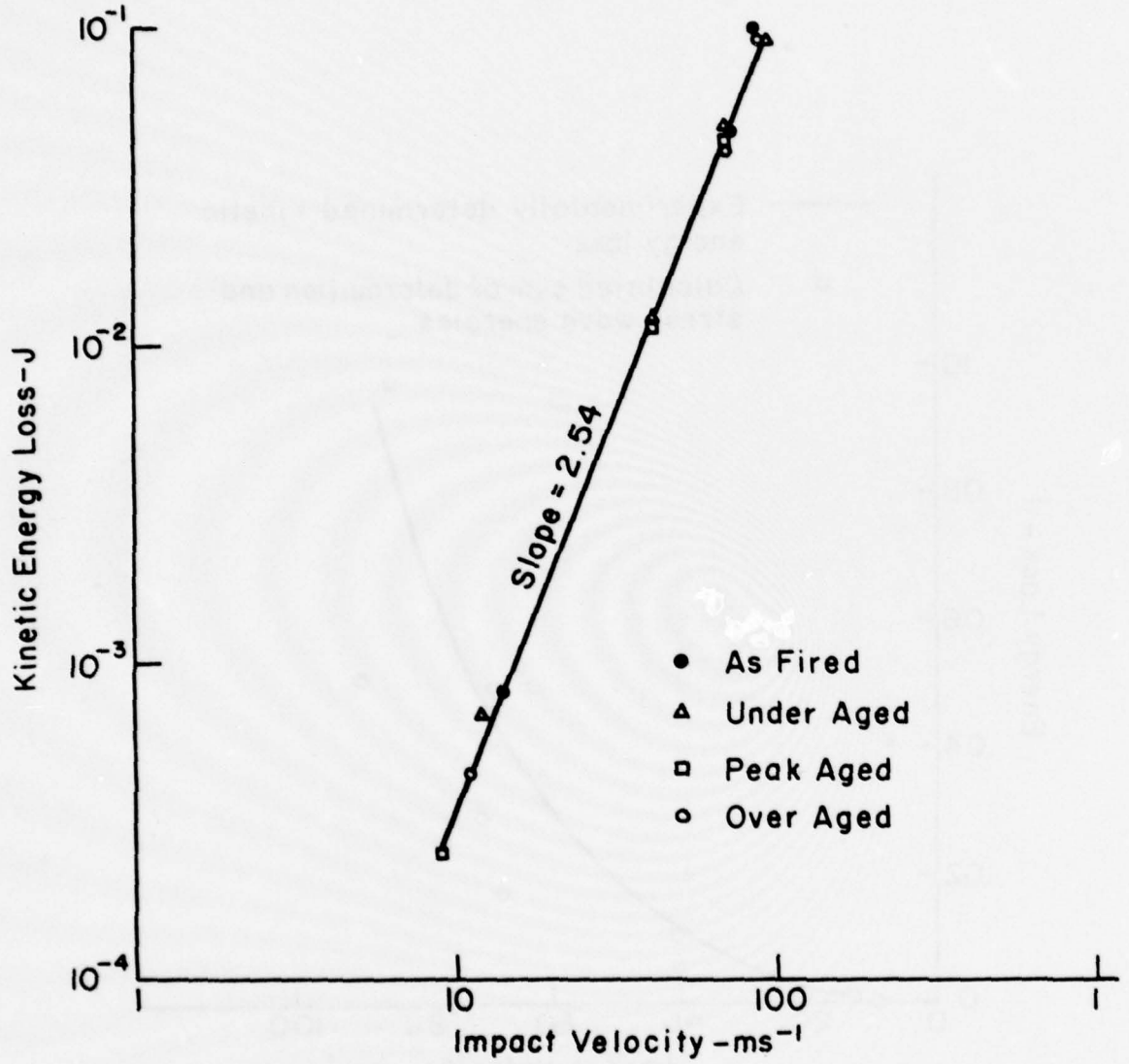


Figure 5 Kinetic Energy Loss vs. Impact Velocity for TT ZrO_2 Impacted by 1.588 mm. Diameter Tungsten Carbide Spheres

$$\Delta U_k = U_i - U_e + U_{sw} \tag{2}$$

By comparing estimates of ΔU_k with the sum of the terms on the right hand side of Equation (2) one can determine whether or not the important loss mechanisms have been accounted for.

U_i was estimated by static indentation tests. Tungsten carbide spheres were loaded to successively higher loads and the radius of the indentation was measured at each step. Assuming a spherical indentation, the penetration (or depth) was calculated for each load and a load vs. penetration curve was plotted. Integration of the load vs. penetration curve yielded an indentation energy vs. penetration curve.

U_{sw} was assumed to be the only energy loss mechanism at velocities near zero. U_{sw} near zero velocity was estimated by extrapolating the curve in Figure 3 to the vertical axis and calculating the kinetic energy loss. At low velocities U_{sw} is approximately 14% of the impact energy. At higher impact velocities U_{sw} was assumed to be a constant fraction of the kinetic energy determined by

$$U_{sw} = (1 - e_o^2)\ \frac{1}{2}\ mv^2 \tag{3}$$

in which e_o is the coefficient of restitution near zero velocity, m is the mass of the sphere and v is the velocity.

The results of calculations for individual impacts are plotted as open circles in Figure 4 and representative values are given in Table I. Even though the results are scattered, the above calculations show that it is reasonable to assume that deformation and stress wave energies comprise the major energy losses. At high impact velocities the energy of plastic deformation (U_p) becomes the dominant loss mechanism, contributing more than 80% of the total.

TABLE I

Partitioning of Impact Energy
(As Fired TT-ZrO_2)

Impact Velocity ms^{-1}	13.9	71.4	85.1
		Joules	
Impact Energy (U_k)	.00307	.0811	.1150
Rebound Energy	.00225	.0345	.0162
Energy Loss (ΔKE)	.00082	.0466	.0998
Indentation Energy (U_i)	.00167	.0525	.0974
Plastic Deformation Energy (U_p)	.00018	.0180	.0812
Stress Wave Energy (U_{sw})	.00044	.0117	.0166

Impact damage and strength degradation

Goodier, as cited by Evans[16], found that the plastic penetration (indentation depth) q of a projectile can be expressed for small penetrations by

$$\frac{q}{r_p} = \delta \, v \sqrt{\frac{\rho_p}{H}} \qquad (4)$$

where r_p is the radius of the projectile, v is the projectile velocity, ρ_p is the projectile density, H is the hardness of the target and δ is a constant. In the present case the projectile and target properties are constant and can be combined with δ to yield the prediction that the penetration is proportional to the velocity.

The penetration depths were calculated from the indentation radii using the assumption of spherical indentations and plotted versus the impact velocity as shown in Figure 6. The penetration increases linearly with velocity as expected and may be extrapolated through the origin. This observation implies that the 1.588 mm tungsten carbide spheres act as sharp indenters, i.e. the yield stress is exceeded at all impact velocities.

At impact velocities over about 25 ms^{-1} radial cracks were observed in all cases. The number of radial cracks was counted and is plotted versus the indentation radius in Figure 7. Extrapolation of the sparse data indicates that at indentation radii less than 130-150 μm one should not observe radial crack formation. In fact, indentations with radii of 107-124 μm did not show radial crack formation.

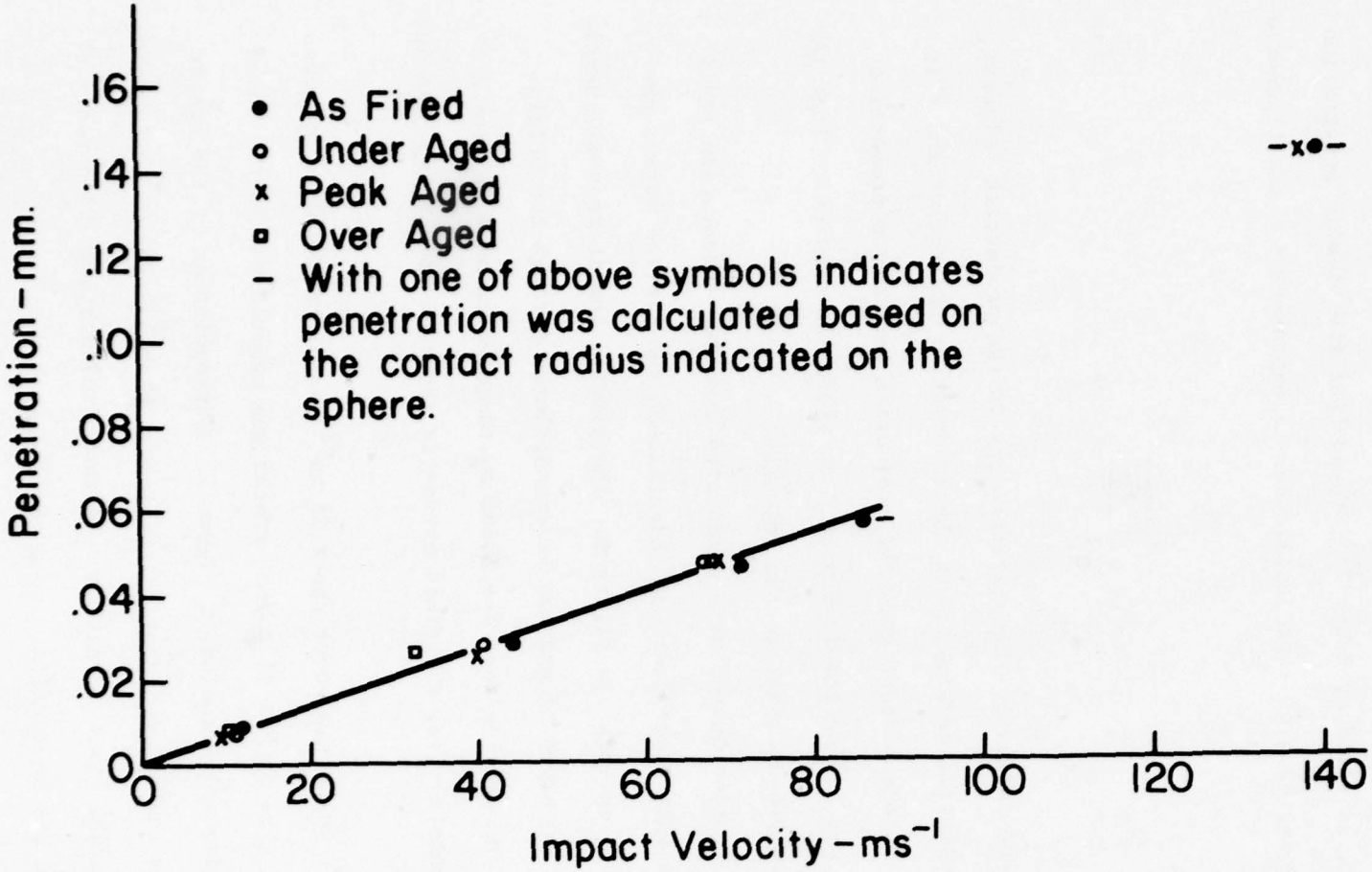


Figure 6 Penetration (Indentation Depth) vs. Impact Velocity for Impacts of Tungsten Carbide Sphere on TT ZrO_2

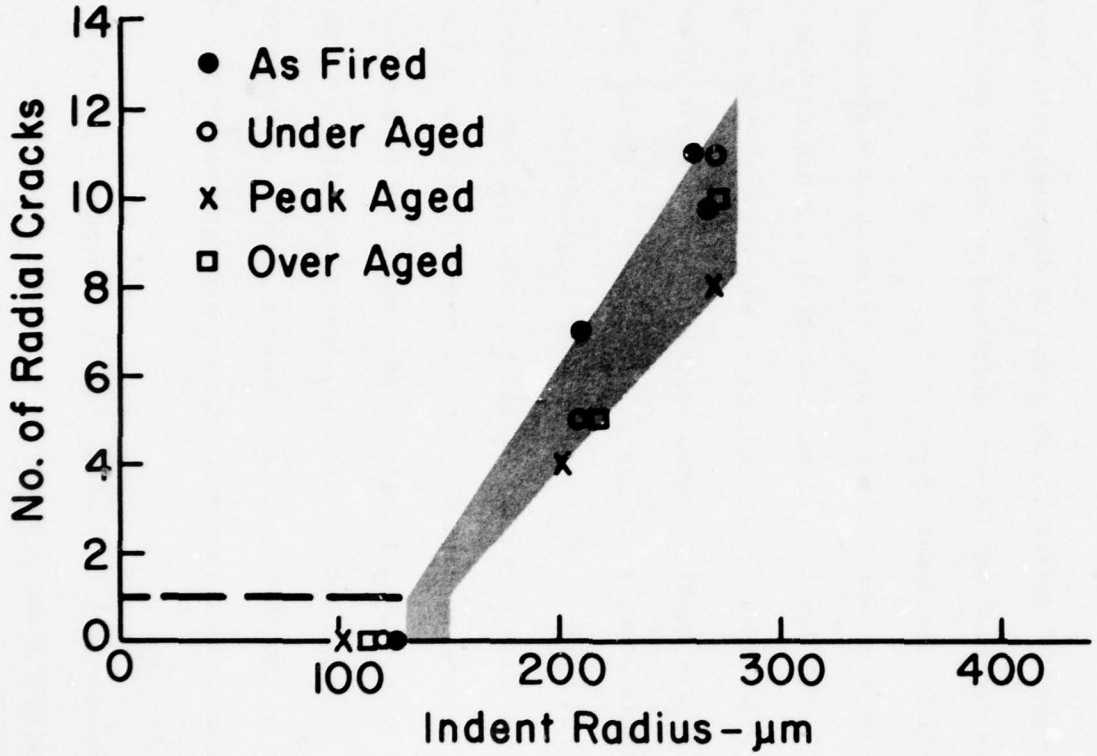


Figure 7 No. of Radial Cracks vs. Indent Radius for Impacts of 1.588 mm. Diameter Spheres on TT ZrO_2

Lange and Evans[17] impacted yttria stabilized zirconia using 400 μm tungsten carbide spheres at velocities up to 750 ms^{-1} and observed no radial crack formation. The absence of radial cracks may possibly be explained by insufficient strain at the boundary for very small indentations.

The number of radial cracks seems to decrease with increasing aging time. This decrease may have an important effect on the strength degradation as will be discussed later.

The length of the longest radial crack in each specimen was measured. The radial crack lengths are plotted versus the impact velocities in Figure 8. The radial crack lengths of specimens with the various aging times are nearly equal at given velocities up to about 70 ms^{-1}. This observation is contrary to expectations based on the K_{IC} values of the materials and will be discussed in more detail later.

The remaining strengths of the impacted specimens were measured (one bar for each test condition) by three point loading on a one inch span with the impact site on the tensile surface under the center load point. The strengths decreased with increasing impact velocity, as expected (Figure 9). The shapes of the curves for the various aging treatments were similar. Each treatment maintained its relative strength advantage, approximately, at each velocity.

K_{IC} values were estimated from the fracture stresses and measured flaw sizes, for a small number of specimens with rather small flaw sizes with the results shown in Table I. The K_{IC} values increase with aging time as expected but the values are somewhat lower than those obtained by the SENB method. In interpreting these results it should be remembered

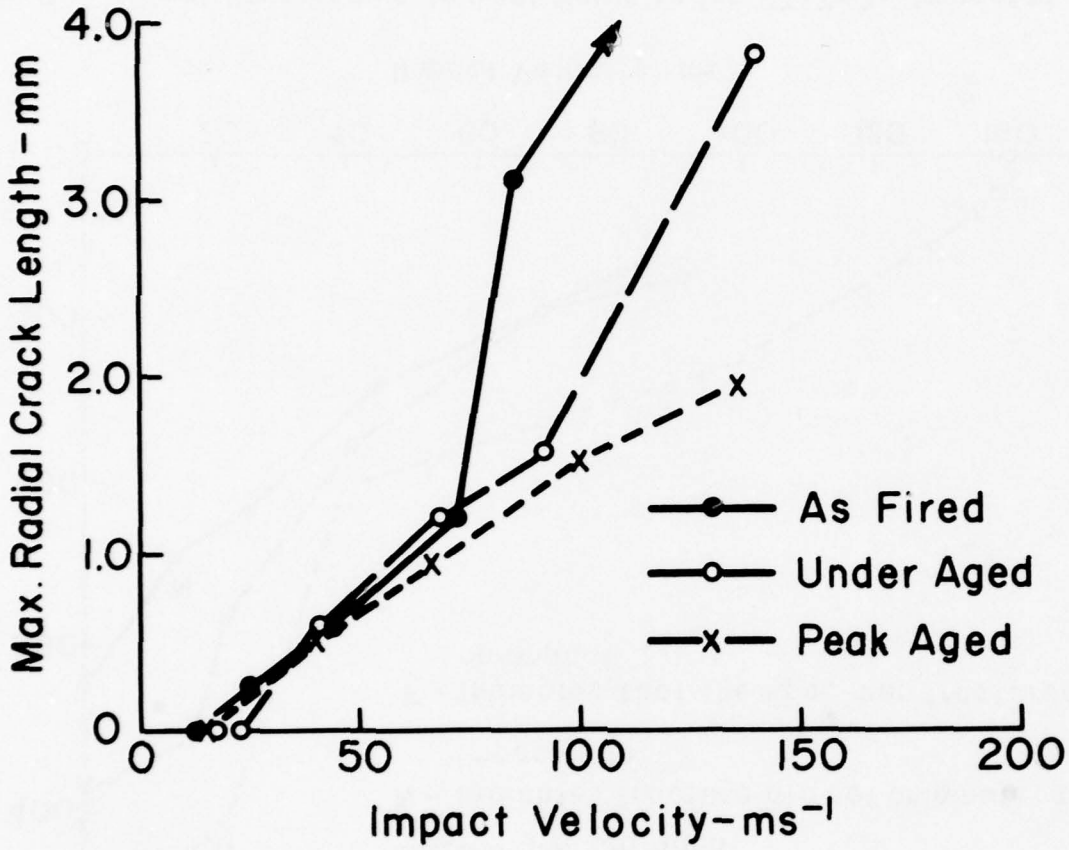


Figure 8 Radial Crack Length vs. Impact Velocity for TT ZrO_2

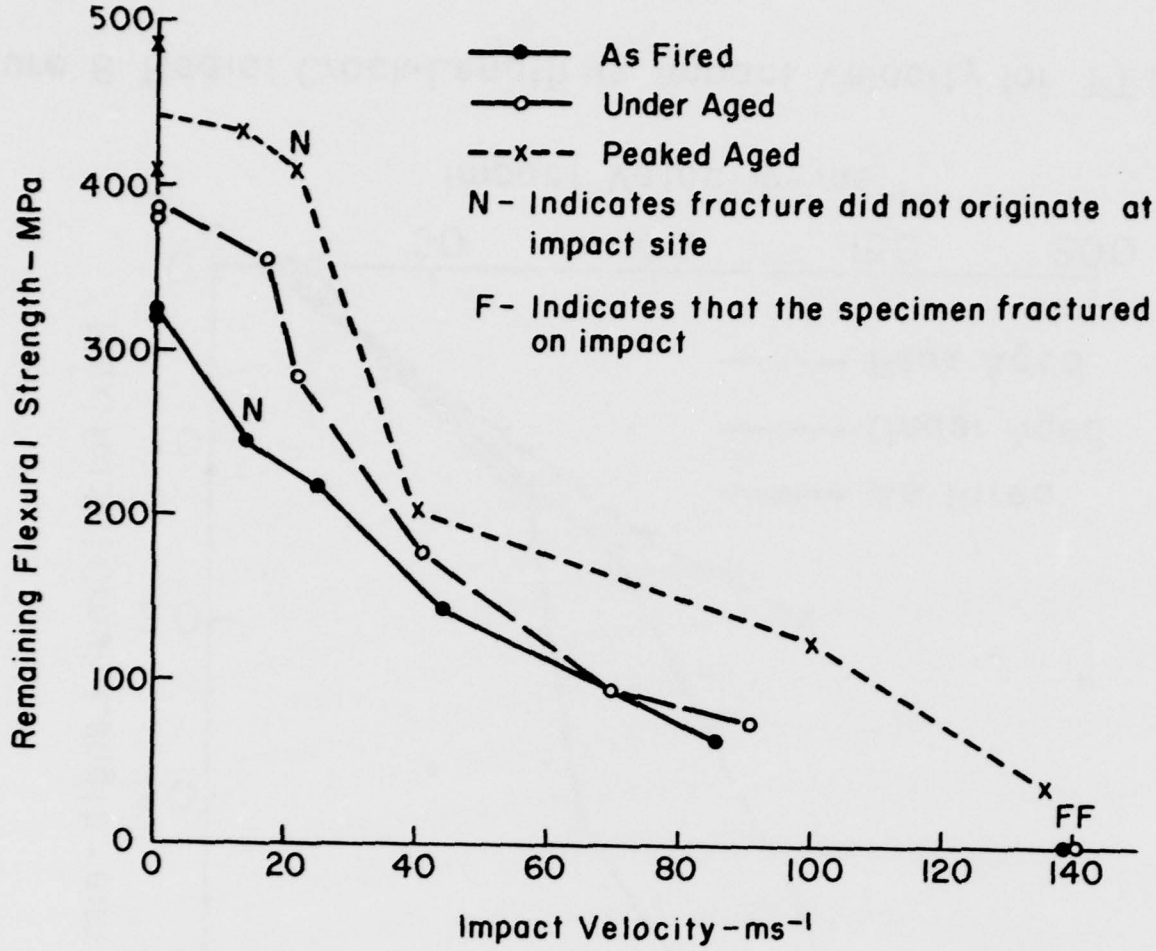


Figure 9 Flexural Strength vs. Impact Velocity for TT ZrO_2 Impacted by 1.588 mm. diam. Tungsten Carbide Spheres

Table I. K_{IC} Values Estimated from Flaw Radius* and SENB Measurements.

Treatment	Fracture Origin	Fracture Stress MPa	Flaw Radius μm	Est. K_{IC} MPam$^{1/2}$	SENB Method K_{IC} MPam$^{1/2}$	Average K_{IC} MPam$^{1/2}$
As-Fired	Radial Crack	219	250	4.7	5.5	5.1
Under-aged	Possible Cone Crack	357	300	6.1	7.6	6.9
Peak-aged	Possible Cone Crack	438	300	7.5	10.5	9.0

*The flaws were assumed to be semi-circular and the K_{IC} values were calculated as follows:

(1) For the radial cracks the fracture was assumed to originate at the surface. The surface correction (1.2) was chosen from Figure 4 of Smith, Emery and Kobayashi[18] leading to $K_{IC} = 1.35\ \sigma_F\ C^{1/2}$ where σ_F is the fracture stress and C is the flaw radius.

(2) For the possible cone cracks, the fracture was assumed to originate at the deepest disturbed material. The variability of the stress field was corrected for using correction factors selected from Figure 6 of Smith, Emery and Kobayashi[18].

that these K_{IC} values are based on preexisting flaw measurements but substantial subcritical crack growth may have occurred leading to critical flaws larger than those measured. Therefore, these estimates of K_{IC} may be smaller than the actual values. To obtain final estimates of K_{IC}, the SENB results which are thought to be too high and those based on the flaw measurements which are thought to be too low were averaged yielding the results which are included in Table I.

As noted in Table I, Griffith-Irwin fracture mechanics can be used to calculate the fracture stresses of specimens with flaws of known sizes and shapes. The basic equation can be written as

$$K_{IC} = Y \ \sigma_F \ C^{1/2} \tag{5}$$

in which Y is a factor which accounts for the flaw shape and proximity to the surface, σ_F is the fracture stress, and C is the flaw size, usually the flaw depth. Lawn and Marshall[19] have related the depth of damage induced by contact stresses to the load (P) and K_{IC} by dimensional analyses as

$$K_{IC} = \chi \frac{P}{C^{3/2}} \tag{6}$$

in which χ is a dimensionless contact constant. Combining these equations to eliminate C yields

$$\sigma_F = \frac{K_{IC}^{4/3}}{Y \ \chi^{1/3} \ P^{1/3}} \tag{7}$$

Equation (7) leads one to expect that, if P is constant for the various materials impacted at a particular velocity, $\sigma_F \propto K_{IC}^{4/3}$. Using the average K_{IC} values in Table I, one would expect the fracture stresses of the peak-aged specimens to be slightly more than twice those of the as-fired specimens but the differences are less than that. This difference can be accounted for by two factors. First, the loads exerted on the under-aged and peak-aged materials at a given velocity are slightly greater (15-25%) than the loads exerted on the as-fired material. Second, the smaller number of radial cracks in the peak-aged material as compared to the as-fired leads to higher stress intensity values at a given radial crack length* so that the radial cracks in the peak-aged material will tend to be longer than otherwise expected. The effect of the number of radial cracks on the stress intensity factor is not accounted for in the theory.

Based on Equation (7) one would expect the remaining strength of a particular material impacted by a particular projectile to vary linearly with $P^{-1/3}$. In the present case, one would expect three curves with different slopes because the three materials have different K_{IC} values. The sparse data (Figure 10) are evidently not sufficient to demonstrate this last effect, but the data taken together show a linear relationship although the curve does not pass through the origin. Using reasonable estimates of Y and χ, (Y = 1.11, χ = .102), and the measured slope yields an estimate of K_{IC} which was 8.6 $MPam^{1/2}$, a value in the range of the measured values.

---

*It is well known that the presence of other cracks can, in some cases, reduce the stress intensity factor at the tip of a particular crack. The authors are not aware of a solution for radiating semi-circular cracks. However, Tada, Paris and Irwin[20] contains a solution for radiating straight-through cracks. In this case, for more than ten radial cracks the ratio of the stress intensity factor for n radial cracks compared with that for one such crack is approximately $2/\sqrt{n}$.

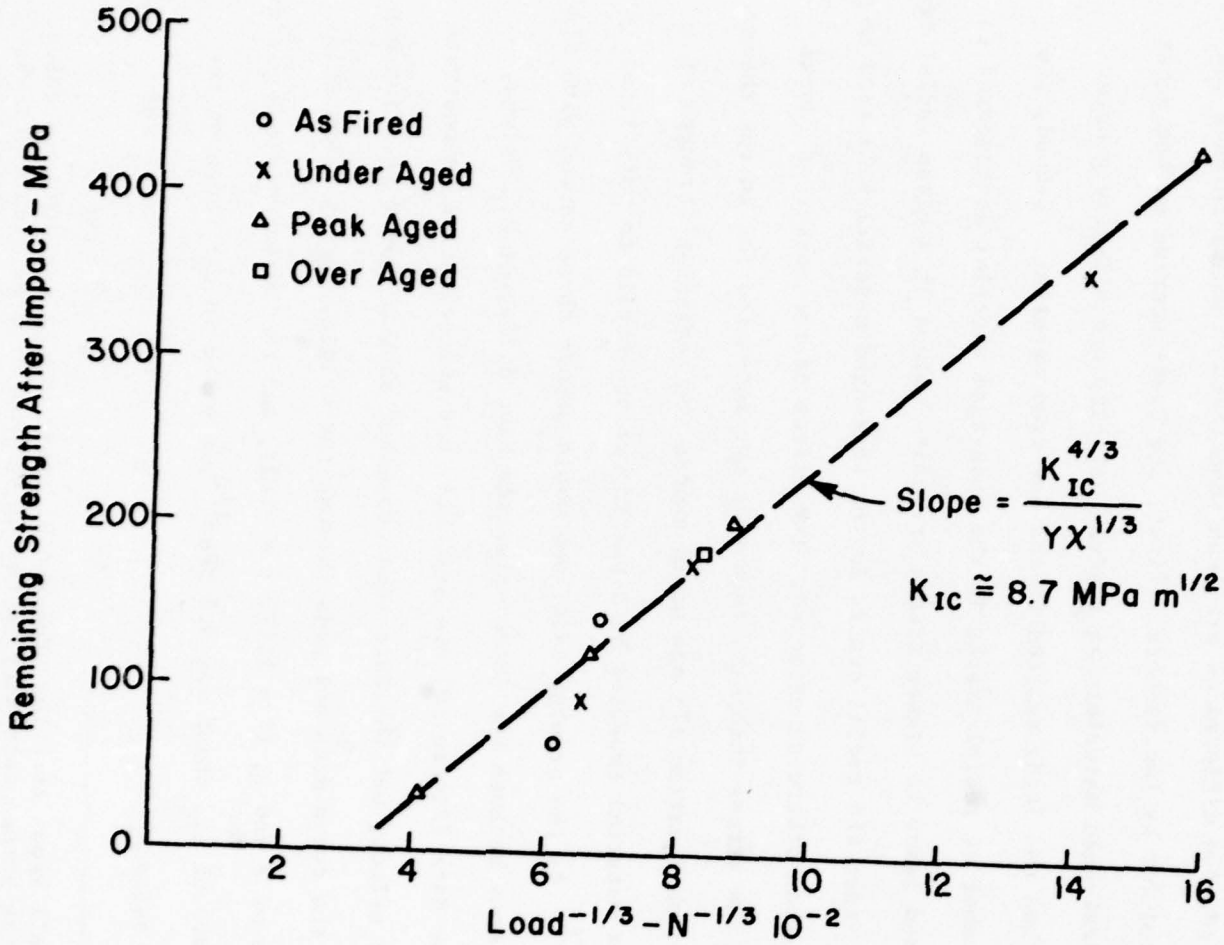


Figure 10 Load$^{-1/3}$ vs Remaining Strength After Impact for TT ZrO_2

IV. Conclusions

TT ZrO_2 is resistant to localized impact damage by glass and steel spheres. 3 mm diameter glass spheres impacting at velocities up to 124 ms^{-1} and 1.59 mm diameter steel spheres impacting at velocities up to 198 ms^{-1} did not cause visible damage. Harder tungsten carbide spheres, 1.59 mm diameter, indented the surfaces at impact velocities as low as 9 ms^{-1} showing an elastic plastic response. At higher impact velocities radial, circumferential and lateral vent cracks were observed, in addition to the indentations.

The energy loss during impact was analyzed. The work of plastic deformation accounts for most of the energy loss at high velocities. Most of the remaining energy loss can be accounted for by the stress wave energy.

The remaining strengths of the TT ZrO_2 specimens with three aging treatments decreased with increasing impact velocity, as expected. At a particular impact velocity, the remaining strength increased with increasing aging time (K_{IC}) but the increase was somewhat less than expected. This difference can be accounted for by the slightly greater loads on the higher K_{IC} specimens and the formation of fewer radial cracks. Higher loads and reduced number of radial cracks yield higher stress intensity factors and greater crack propagation than otherwise expected.

References

1. R. C. Garvie, R. H. Hannink and R. T. Pascoe, "Ceramic Steel?", Nature 258, 703-704 (Dec. 25, 1975).

2. R. C. Garvie, R. H. J. Hannink, R. R. Hughan, N. A. McKinnon, R. T. Pascoe and R. K. Stringer, "Strong and Partially Stabilized Zirconia Ceramics," J. Australian Ceramic Society 13 (1) 8-11 (May, 1977).

3. D. L. Porter and A. H. Heuer, "Mechanisms of Toughening Partially Stabilized Zirconia Ceramics (PSZ)," J. Amer. Ceram. Soc. 60 (3-4) 183-184 (1977).

4. R. T. Pascoe and R. H. J. Hannink, "Microstructural Changes During Isothermal Aging of Lime-Stabilized Zirconia," To be submitted for publication.

5. T. Gupta, "Role of Stress-Induced Phase Transformation in Enhancing Strength and Toughness of Zirconia Ceramics," from Fracture Mechanics of Ceramics, Vol. 4, Edited by R. C. Bradt, D. P. H. Hasselman and F. F. Lange, Plenum, New York (1978) p. 877-889.

6. R. T. Pascoe and R. C. Garvie, "Surface Strengthening of Transformation-Toughened Zirconia," Ceramic Microstructures (1976), Proceedings of the 6th International Symposium, Richard M. Fulrath, Editor, Westview Press, Boulder, Colo. (1977).

7. L. A. Simpson, "Microstructural Considerations for the Application of Fracture Mechanics Techniques", from Fracture Mechanics of Ceramics, Vol. 2 Edited by R. C. Bradt, D. P. H. Hasselman and F. F. Lange, Plenum, New York (1974) p. 567-577.

8. R. F. Pabst, "Determination of K_{IC} - Factors With Diamond Saw Cuts in Ceramic Materials," Ibid, p. 555-565.

9. H. P. Kirchner and R. M. Gruver, "Localized Impact Damage in Stressed Al_2O_3 and Si_3N_4," Mater. Sci. and Eng. 34 (1) 25-31 (1978).

10. D. B. Marshall, B. R. Lawn, H. P. Kirchner and R. M. Gruver, "Contact-Induced Strength Degradation of Thermally Treated Al_2O_3," J. Amer. Ceram. Soc. 61 (5-6) 271-272 (1978).

11. J. J. Gilman, "Hardness-A Strength Microprobe," from The Science of Hardness Testing and Research Applications," Edited by J. H. Westbrook and H. Conrad, American Society for Metals, Metals Park, Ohio (1973), p. 51-74.

12. H. P. Kirchner and R. M. Gruver, "Localized Impact Damage in Glass," Mater. Sci. Eng. 28, 153-160 (1977).

13. H. P. Kirchner and R. M. Gruver, "Localized Impact Damage in a Viscous Medium (Glass)," from Fracture Mechanics of Ceramics, Vol. 3, Edited by R. C. Bradt, D. P. H. Hasselman and F. F. Lange, Plenum (1978), p. 365-377.

14. S. C. Hunter, "Energy Absorbed by Elastic Waves During Impact," J. Mech. Phys, Solids 5, 162-171 (1957).

15. H. P. Kirchner and R. M. Gruver, "The Effect of Localized Damage on Energy Losses During Impact," Mater. Sci. Eng. 33 (1) 101-106 (1978).

16. A. G. Evans, "Impact Damage in Ceramics," from Fracture Mechanics of Ceramics, Vol. 3, Edited by R. C. Bradt, D. P. H. Hasselman and F. F. Lange, Plenum, New York (1978), pages 303-331.

17. F. F. Lange and A. G. Evans, "Erosive Damage Depth in Ceramics: A Study on Metastable, Tetragonal Zirconia," Submitted for publication.

18. F. W. Smith, A. F. Emery, and A. S. Kobayashi, "Stress Intensity Factors for Semi-Circular Cracks, Part 2-Semi-Infinite Solid," J. Appl. Mech. 34 Series E, 953-959 (December, 1967).

19. B. R. Lawn and D. B. Marshall, "Contact Fracture Resistance of Physically and Chemically Tempered Glass Plates: A Theoretical Model," Phys. Chem. Glasses 18 (1) 7-18 (1977).

20. H. Tada, P. Paris, and G. Irwin, "The Stress Analysis of Cracks Handbook," Del Research Corp., Hellertown, PA (1973), p. 21.5.

Crack Propagation and Branching in Transformation Toughened Zirconia

by

H. P. Kirchner*
R. M. Gruver*
R. C. Garvie**

* Ceramic Finishing Co., State College, PA, U.S.A.
** CSIRO, Division of Materials Science, Melbourne, Australia

Acknowledgements

The authors are pleased to acknowledge the contributions of their associates at CSIRO and Ceramic Finishing Company and the sponsorship of the Office of Naval Research.

Abstract

Crack propagation and branching were investigated in calcia partially stabilized zirconia aged at 1300°C for various times. The stress intensity factor at crack branching increased with increasing aging time. The strain intensity criterion for crack branching was used to estimate the effective crack tip radius at branching and the increase in this radius attributable to the transformation toughening mechanism.

I. Introduction

In brittle materials there is an orderly progression of fracture features along lines drawn radially in the fracture surface from the fracture origin. These features include a flat region usually referred to as the mirror, a mist region, a region of radiating ridges and valleys called hackle and a boundary at which large scale crack branching occurs. In this paper large scale crack branching is simply called crack branching and is to be distinguished from microbranching. Crack branching occurs at a particular value of stress intensity factor and is a response to large scale stresses and macro properties. Micro-branching is considered to be a response to localized stresses and material property variations.

The fracture stress (σ_F) and the radius to the crack branching boundary (C_B) can be related by[1-4]

$$K_B = Y\sigma_F C_B^{1/2} \tag{1}$$

in which K_B is the stress intensity factor at crack branching and Y is the appropriate geometrical factor for the crack at branching. K_B can be determined by plotting σ_F vs $C_B^{-1/2}$ and determining the slope which is K_B/Y.

The fracture toughness of zirconia can be increased by proper control of composition and heat treatment[5-7]. When calcia partially stabilized zirconia is aged at intermediate temperatures (1200-1500°C) in the cubic-tetragonal phase field, the tetragonal precipitate in the much larger cubic crystals is coarsened[8]. At lower temperatures the tetragonal phase becomes increasingly susceptible to transformation to the monoclinic phase. Tensile stress favors this transformation because the monoclinic phase is less dense than the tetragonal. Therefore, when cracks propagate through the material

the tensile stress, concentrated at the crack tip, causes the tetragonal crystals within a few micrometers of the crack to transform to monoclinic[9]. This transformation increases the critical stress intensity factor (K_{IC}) so that the material is sometimes called transformation toughened zirconia ($TTZrO_2$).

The mechanism responsible for the increase in fracture toughness with increasing transformation from the tetragonal to the monoclinic is not completely understood[7,10-18]. In some cases the individual crystals are considered to act as barriers to crack propagation[13] or as a source of microcrack formation[11,14] and, in other cases, it is assumed that the expansion that occurs with formation of the monoclinic phase absorbs energy and acts to reduce elastic strain at the crack tip[16,17].

The factors determining K_B in a particular ceramic material and the relationship of K_B to K_{IC} also are not understood completely. In most ceramics, the K_{IC} does not vary much from the value one might expect based on the variation of Young's modulus. This lack of variability has made it difficult to study toughening mechanisms and the relationship of K_B to K_{IC} in ceramics. Because of the high strength and fracture toughness of $TTZrO_2$ and the fact that these properties can be varied by heat treatment, with little change in Young's modulus, it was of interest to study crack propagation and crack branching in $TT\text{-}ZrO_2$.

II. Procedures

Calcia partially stabilized ZrO_2 with four 1300°C aging treatments (as-fired, 0 hours; under-aged, 30 hours; peak-aged, 48 hours; and over-aged, 57 hours) was prepared at CSIRO in the form of rectangular bars, 3 x 10 x 40mm, with ground (50 grit) surfaces. At Ceramic Finishing Company one large surface of each bar was polished on a paper covered rotating lap. Polishing removed most of the monoclinic phase induced in the surface by grinding and the resulting compressive surface layer[19]. Diamond polishing was more effective than alumina polishing in reducing the monoclinic content of the surface.

The specimens analyzed in this investigation were originally fractured in an investigation of strength degradation due to localized impact damage[19]. The specimens that were analyzed were those that fractured at relatively high stresses; that is, the controls that were not impacted and the specimens with minimal impact damage. Only those specimens showed crack branching. The specimens were tested in flexure by three point loading on a one inch span.

The fracture surfaces of the specimens were characterized. The following criteria were used to locate the fracture origins:

1. The center of area of reflecting spots which were observed by optical microscopy with the specimen illuminated at the proper angle.
2. The center of semi-circle formed by flakes of uniform size.
3. The intersection of lines extended through the mirror region parallel to the hackle.
4. The center of the smooth, relatively flat area (fracture mirror).

The following features were characterized; fracture origin, reflecting spots, crack branching and microbranching. The radii at crack branching were measured

using an optical microscope with a calibrated eyepiece. The measurements were made on the tensile surface where the crack propagates in a uniform stress field.

K_B was calculated as described in Section 1. Y was assumed to be 1.38 which is the value determined by Smith, Emery and Kobayashi[20] for the greatest K_I at the boundary of a semi-circular surface flaw. In some cases, the fractures originated near corners. One might question, whether or not the presence of the additional free surface would significantly increase the stress intensity factors in these cases. However, as shown by Liu[21], this increase is small.

III. Results

Characterization of fracture surfaces

The reflecting spots were the principal features used to locate the fracture origins. In many cases, the locations of the origins were confirmed using the other criteria listed in the previous section. The reflecting spots are cleavage faces of the zirconia grains and are similar to those observed at fracture origins in alumina ceramics[22,23]. However, the grain size of the zirconia is very large (~ 50μm) so the reflecting spots are correspondingly large. In some cases the reflecting surfaces appear to consist of fan shaped segments that are oriented at slightly varying angles to the incident light so that slight changes in specimen orientation are necessary to bring the individual segments into reflecting position. Because the grain size is so large, only a few reflecting spots are observed at the fracture origin.

In a small number of cases, the flaw at the fracture origin was large enough to be identified and characterized. In most cases, the particular flaw at which the fracture originated was not identified.

The fracture surface near a fracture origin is illustrated in Figure 1. The fracture origin was a large pore. This fracture surface was chosen because identification of the flaw at the fracture origin was certain. The fracture is almost entirely transgranular. The fracture origin is surrounded by a relatively flat region containing some radiating lines that may be steps formed by twisting of the crack. The flat region is surrounded by a wavy region beginning at about 0.4mm from the fracture origin. The wavy region becomes increasingly rough as the distance from the fracture origin increases.

The interiors of pores and grain boundaries exposed by fracture frequently show very uniform surface roughness in limited areas (Figure 2).

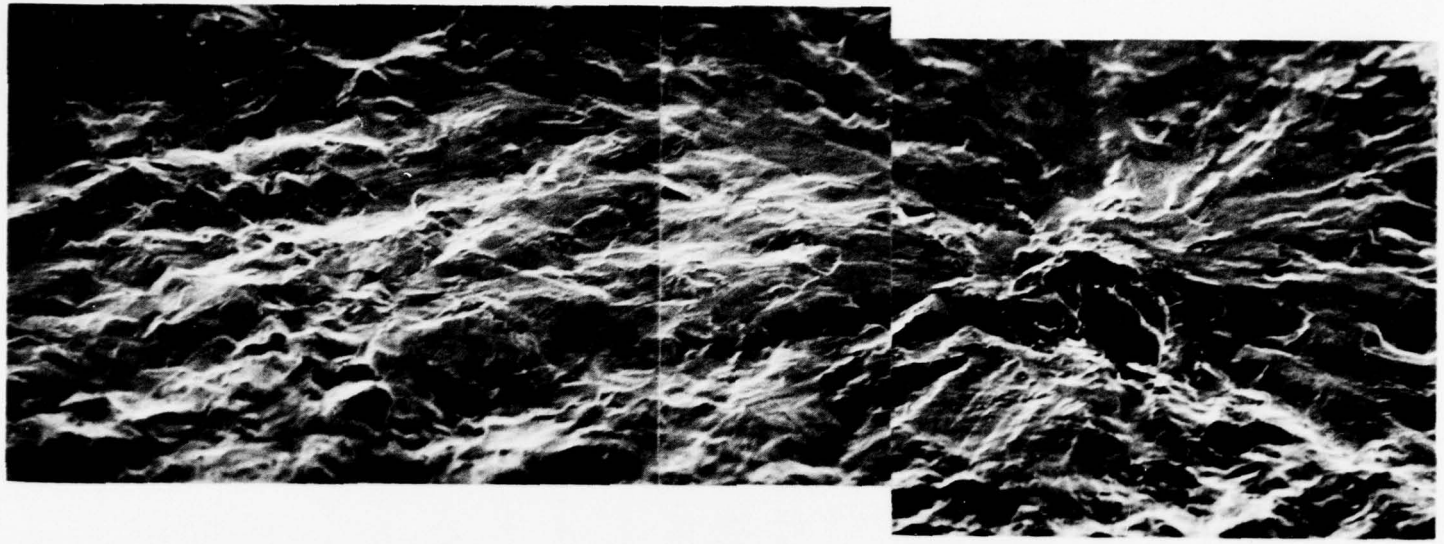


Figure 1 Composite photograph of fracture surface for a fracture originating at a pore. The photograph extends to about 1500 μm from pore (Specimen PA-3, 100X).



Figure 2 Localized surface roughness in a pore.
(Specimen PA-3, 1500X)

This roughness is believed to result from the presence of the precipitate in the larger cubic grains. The presence of the grain boundary roughness may explain the resistance to intergranular fracture that results in the almost complete absence of intergranular fracture near fracture origins.

At distances ranging from about one to four millimeters from the fracture origin, depending on fracture stress and aging time, the first crack branching was observed. Unlike most ceramics in which branching is observed, the TT-ZrO_2 specimens fractured in two halves rather than forming a number of wedge shaped fragments in addition to the two end pieces. Apparently the increased microbranching and K_I at crack arrest in the TT-ZrO_2 prevent the branches from propagating to the point that the wedge shaped pieces can separate from the two halves. The branching can be observed in the tensile surfaces of the specimens under inclined illumination. The edges of the cracks appear to be slightly raised so that they can be seen clearly. Frequently, two or more branches are observed at nearly equal intervals from the fracture origin.

The branches were also observable on the fracture surface. Because the TT-ZrO_2 is rather transparent, light is transmitted through the edges of the wedges formed by branching and reflected from the far surface so that the branches, near their origins, appear as irregular light colored bands.

A branch formed in the tensile surface of a peak-aged specimen fractured at a relatively high stress of 516MPa is illustrated in Figure 3. In the photograph the edge formed by the main crack is approximately horizontal and the branch slopes downward at a branching angle of about 25°. The wedge shaped piece formed by the branch did not separate from the rest of the specimen. The microbranching along the branch is evident.

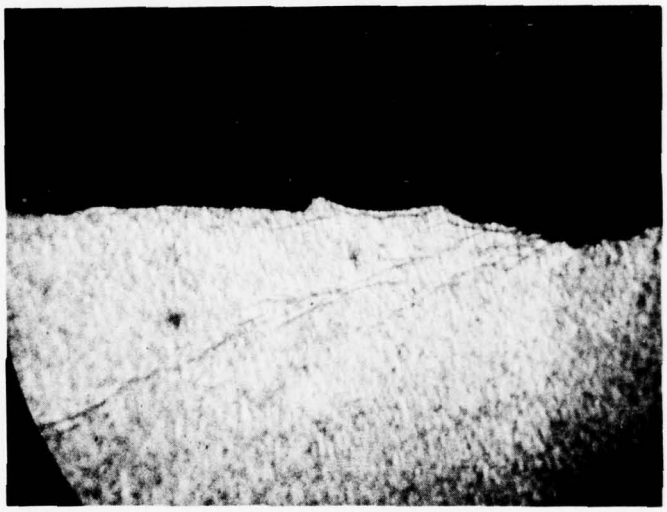


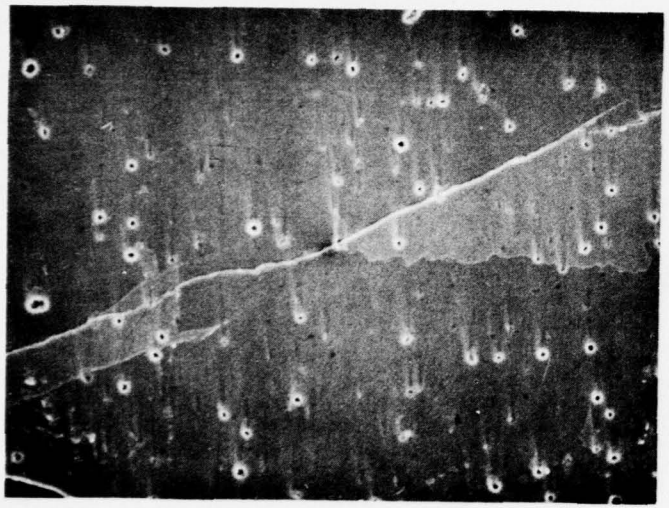
Figure 3 Branching in peak-aged TT-ZrO_2 (Specimen PA-1, fracture stress 516 MPa, 43X).

In the optical microscope, raised edges of the cracks in TT-ZrO_2 cast a shadow that makes the cracks visible. Various attempts have been made to observe these features in the SEM but little progress has been made. A typical result is illustrated in Figure 4 which shows cracks that propagated across a relatively smooth surface with microbranching at the centers of the photographs. At the higher magnification and 45° incidence it appears that the material in the wedge between the microbranches is raised slightly above the original surface. A more ridge-like feature extending along the cracks caused by the volume expansion during the phase transformation had been anticipated but this has not yet been observed.

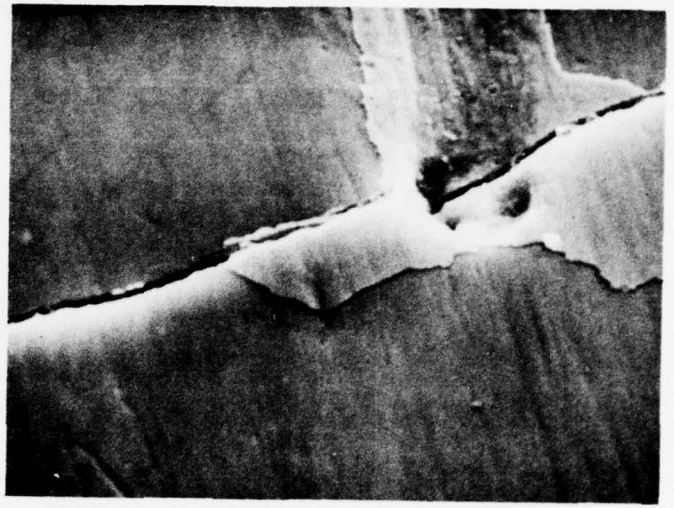
Microbranching is common in these materials. As the crack grows microbranching is first observed near the first large scale branching. Thereafter, microbranching is observed more or less continually along the branches. These observations suggest that the stress intensity factor for microbranching is close to K_B. Furthermore, the absence of microbranching near fracture origins indicates that other mechanisms are responsible for the toughening. It should be emphasized that, although fracture mechanisms that occur when $K_I > K_{IC}$ are interesting in their own right, they cannot provide evidence about toughening mechanisms. This evidence can only be obtained by observations of the fracture surface where $K_I \leq K_{IC}$.

Crack branching measurements and calculation of K_B

The crack branching radii were measured and plotted as suggested by equa. (1) in Figure 5. The data for the various aging times fall into three groups yielding slopes that increase with aging time. K_B was calculated from the data. The average K_B values for various aging times and surface finishes are given in Table I.



A. Perpendicular incidence, 300X



B. 45° incidence, 5000X

Figure 4 Branched crack in peak aged TT - ZrO_2 (Specimen PA-1).

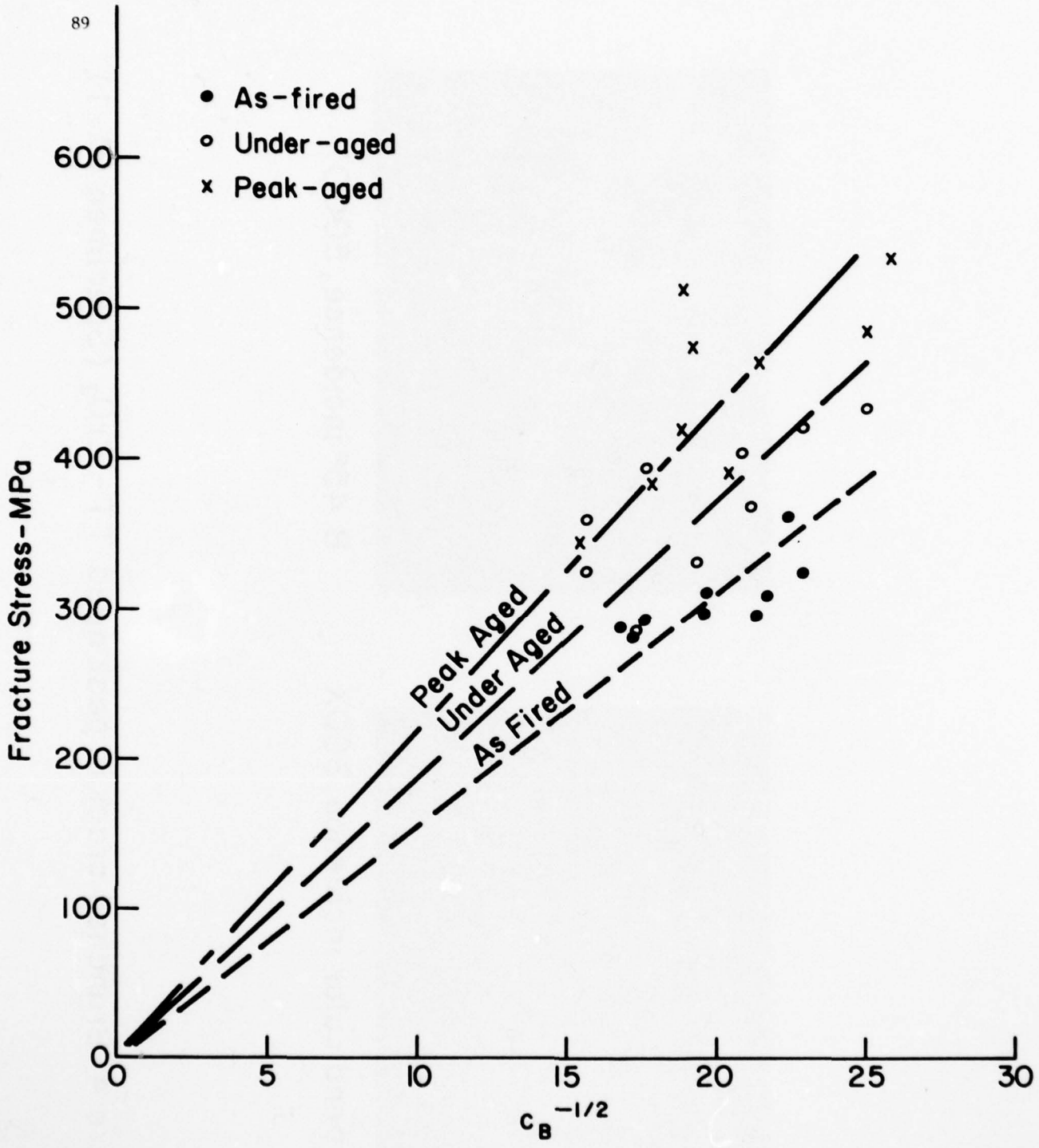


Figure 5 Fracture Stress vs. $c_B^{-1/2}$ for TT-ZrO_2 Specimens with Various Aging Treatments (Combined Data for Three Different Surface Finishes).

TABLE I

Average K_B Values for TT-ZrO_2 Specimens with Various Aging Treatments and Surface Finishes

Surface Finish	Aging Treatment: As-Fired* (0 hours)	Under-Aged* (30 hours)	Peak-Aged* (48 hours)	Over-Aged** (57 hours)
	Average K_B - $MPam^{1/2}$			
As Ground (50 grit)	20.2	23.9	31.0	35.5
Polished (alumina)	22.9	28.6	31.3	31.3
Polished (1/4 μm diamond)	21.1	26.9	29.3	38
Average	21.4	26.5	30.5	34.9

* Three specimens per group

** One specimen per group

IV. Discussion of Results

Evaluation of the effect of residual compressive surface stresses on crack branching

Analysis of crack branching data in cases in which large scale residual stresses can be present must begin with a determination of the importance of these stresses and a decision on how to account for this added complication[3]. The presence of residual compressive surface stresses (σ_R) decreases the nominal applied stress (σ_N) acting at the fracture. Therefore, the fracture stress (σ_F) is algebraic sum of the stresses as in

$$\sigma_F = \sigma_N + \sigma_R \tag{2}$$

where compressive stresses are negative. Substituting in equa. (1) yields

$$K_B = Y(\sigma_N + \sigma_R)C_B^{1/2} \tag{3}$$

Flexural strength measurements consistently show that the strengths of TT-ZrO_2 specimens increase when they are ground and decrease when they are polished[5]. This same effect was observed in the present specimens as shown in Table II. The greatest strength difference (98MPa) is observed for the peak aged specimens which are most susceptible to the tetragonal to monoclinic phase transformation. Pasco and Garvie[23] attribute the strengthening to a compressive surface layer, 20-30μm in depth, that is generated by abrasion and removed by polishing.

The K_B data in Table I which were calculated using σ_N show little variation with the surface finish. This result was surprising in view of the rather large strength differences but it may be caused by the fact that the stressed layers are very thin. In any case, for the remainder of the analysis it is assumed that $\sigma_F = \sigma_N$.

TABLE II

Average Flexural Strengths of TT-ZrO_2 Specimens with Various Aging Treatments and Surface Finishes

Surface Finish	Aging Treatment			
	As-Fired	Under-Aged	Peak-Aged	Over-Aged
	Average Flexural Strength* - MPa			
As Ground (50 grit)	341	446	510	234
As Polished (alumina)	326	384	485	206
As Polished (1/4 μm diamond)	325	380	412	204

* Three point loading on a one-inch span

AD-A068 972 CERAMIC FINISHING CO STATE COLLEGE PA F/G 11/2
LOCALIZED IMPACT DAMAGE IN CERAMICS. THEORY OF ELASTIC-PLASTIC --ETC(U)
JAN 79 H P KIRCHNER, D M RICHARD, R C GARVIE N00014-74-0241

UNCLASSIFIED NL

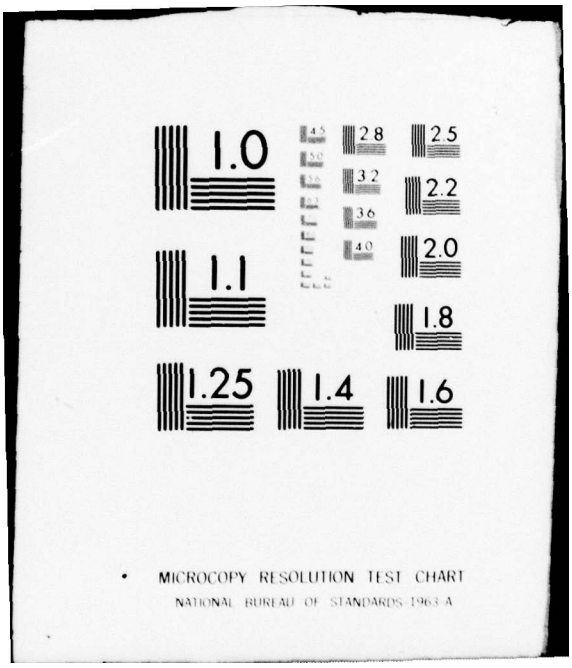
2 OF 2
AD A068972







END
DATE FILMED
7-79
DDC


1.0
1.1
1.25
1.4
1.6
1.8
2.0
2.2
2.5
2.8
3.2
3.6
4.0
MICROCOPY RESOLUTION TEST CHART
NATIONAL BUREAU OF STANDARDS 1963-A

Comparison of K_B and K_{IC} and estimation of effective crack tip radii

K_{IC} values for the TT-ZrO_2 materials were estimated previously by averaging results of single edge notched beam measurements and results calculated from flaw sizes and fracture stresses[19]. These K_{IC} values and the present K_B values are compared in Table III. Probably, the K_{IC} values were not determined accurately enough to merit detailed comparison, as also seems to be the case even for intensively investigated ceramics such as H. P. silicon nitride[24,25]. Nevertheless, it is clear that K_B increases as K_{IC} increases. The Young's moduli of the materials vary only slightly with aging. Because $K_{IC} = (2E\gamma_c)^{1/2}$ where γ_c is the critical fracture energy, it is clear that the increase of K_{IC} with aging is the result of increased fracture energy.

The strain intensity criterion[4] for crack branching can be used to estimate the effective radius (r_e) of the tip of the propagating crack at branching. To do this the strain intensity at crack branching (K_B/E) is calculated and then squared to obtain the estimate of r_e. Earlier results for a large number of brittle ceramics yielded an average r_e of 11×10^{-10}m, a value about 10 times atomic dimensions. The present estimates for TT-ZrO_2 range from 8 to 20 times as great as those previously calculated for more conventional brittle ceramics.

Lange[18] investigated crack propagation in 100% cubic zirconia in which no tetragonal to monoclinic transformation occurs and observed a K_{IC} value of $3MPam^{1/2}$. Comparison of this value with the value for the as-fired material in this investigation ($K_{IC} = 5.1MPam^{1/2}$) indicates that even in the as-fired material transformation toughening is important. If one assumes that, in the absence of the transformation mechanism r_e of ZrO_2 is the same as the average

TABLE III

Comparison of K_B and K_{IC} and Calculation of Effective Radius of Crack Tip

Treatment	Average K_B $MPam^{1/2}$	Average K_{IC} $MPam^{1/2}$	E MPa	$\frac{K_B}{E}$ $m^{1/2}$	$r_e = (\frac{K_B}{E})^2$ m
As-Fired	21.4	5.1	226,000	$9.46 \cdot 10^{-5}$	$9.0 \cdot 10^{-9}$
Under-Aged	26.5	6.9	222,000	$11.9 \cdot 10^{-5}$	$14.2 \cdot 10^{-9}$
Peak-Aged	30.5	9.0	207,000[1]	$14.7 \cdot 10^{-5}$	$21.7 \cdot 10^{-9}$
Over-Aged	34.9	-	-	-	-

Note (1) This value represents an earlier measurement on another batch of material[6]

value for the brittle ceramics investigated previously ($\frac{K_B}{E} = 3.3 \cdot 10^{-5} m^{1/2}$ so that $r_e = 10.9 \cdot 10^{-10}$m), one can estimate the increase in r_e due to the transformation mechanism (for example, for peak-aged TT-ZrO_2 $21.7 \cdot 10^{-9} - 1.05 \cdot 10^{-9} = 20.7 \cdot 10^{-9}$m). It is an interesting question whether or not this change in r_e could be estimated from the volume expansion of the tetragonal to monoclinic transformation, the fraction of tetragonal phase originally present and the variation of the percentage of transformation occurring with distance from the crack surface. This estimate has not been attempted here because of insufficient information on the last two items.

One might question why it is desirable to invoke the strain intensity criterion for crack branching when it is clear from available evidence such as Figure 1 of reference (13) that cracks in TT-ZrO_2 are deflected in many cases by the precipitate particles, indicating that the particles resist crack propagation. The point is that, as shown recently for 96% alumina[22], the increase in K_I, as the crack grows beyond the critical flaw boundary, must be accompanied by absorption of energy by a variety of not yet identified mechanisms. The crack can only absorb a given amount of energy in going around a particular precipitate particle. The remainder must be absorbed by other mechanisms perhaps involving extension of the thickness of the transformed layer. Thus, r_e continues to increase as the crack propagates.

It is important to realize the r_e does not represent the actual radius of the crack tip which remains small. Neither does it represent the radius of the zone in which transformation occurs. Instead it represents the radius the crack tip would have to have if the expansion due to the phase transformation had not occurred but the fracture stress and fracture energy remained the same.

If one views crack branching as a fracture process that occurs when the total elastic strain at the crack tip reaches a critical value sufficient to support propagation of two cracks, it is clear that mechanisms such as phase transformations occurring with an increase in volume, and plastic deformation, will act to reduce the total elastic strain at each particular crack length, postponing crack branching until the elastic strain intensity increases to the point that crack branching can occur.

References

1. A. B. J. Clark and G. R. Irwin, "Crack Propagation Behaviors," Experimental Mechanics 6, 321-330 (June, 1966).

2. J. Congleton and N. J. Petch, "Crack-Branching," Phil. Mag. 16, 749-760 (1967).

3. H. P. Kirchner and R. M. Gruver, "Fracture Mirrors in Alumina Ceramics," Phil. Mag. 27(6) 1433-1446 (1973).

4. H. P. Kirchner, "The Strain Intensity Criterion for Crack Branching in Ceramics," Engineering Fracture Mechanics 10, 283-288 (1978).

5. R. C. Garvie, R. H. Hannink and R. T. Pascoe, "Ceramic Steel?", Nature 258, 703-704 (Dec. 25, 1975).

6. R. C. Garvie, R. H. J. Hannink, R. R. Hughan, N. A. McKinnon, R. T. Pascoe and R. K. Stringer, "Strong and Partially Stabilized Zirconia Ceramics," J. Australian Ceramic Society 13(1) 8-11 (May, 1977).

7. D. L. Porter and A. H. Heuer, "Mechanisms of Toughening Partially Stabilized Zirconia Ceramics (PSZ)," J. Amer. Ceram. Soc. 60(3-4) 183-184 (1977).

8. R. T. Pascoe and R. H. J. Hannink, "Microstructural Changes during Isothermal Aging of Lime Stabilized Zirconia," To be submitted for publication.

9. T. Gupta, "Role of Stress-Induced Phase Transformation in Enhancing Strength and Toughness of Zirconia Ceramics," from Fracture Mechanics of Ceramics, Vol. 4, Edited by R. C. Bradt, D. P. H. Hasselman and F. F. Lange, Plenum, New York (1978), p. 877-889.

10. G. K. Bansal and A. H. Heuer, "Precipitation in Partially Stabilized Zirconia," J. Amer. Ceram. Soc. 58(5-6) 235-238 (1975).

11. N. Claussen, Comments on "Precipitation in Partially Stabilized Zirconia," J. Amer. Ceram. Soc. 59(3-4) 179 (1976).

12. D. L. Porter, G. K. Bansal and A. H. Heuer, "Reply by," J. Amer. Ceram. Soc. 59(304) 179-182 (1976).

13. D. L. Porter and A. H. Heuer, "Mechanisms of Toughening Partially Stabilized Zirconia (PSZ)," J. Amer. Ceram. Soc. 60(3-4) 183-184 (1977).

14. R. W. Rice, "Further Discussion of "Precipitation in Partially Stabilized Zirconia," J. Amer. Ceram. Soc. 60(5-6) 280 (1977).

15. D. L. Porter and A. H. Heuer, "Reply to Further Discussion of "Precipitation in Partially Stabilized Zirconia," J. Amer. Ceram. Soc. 60(5-6) 280-281 (1977).

16. C. A. Andersson and T. K. Gupta, "Martensitic Transformation Toughening of ZrO_2," Paper 83-B-78 Annual Meeting Amer. Ceram. Soc., May 9, 1978.

17. F. F. Lange, "Microstructurally Developed Toughening Mechanisms in Ceramics: I. Theory of Metastable Phase Retention and Contribution to Fracture Toughness," Rockwell International Science Center Technical Report No. 2 (SC 5117.2TR), Contract N00014-77-C-0441 (July, 1978).

18. F. F. Lange, "Stress Induced Martensitic Reaction: II. Experiments in the ZrO_2-Y_2O_3 System," Rockwell International Science Center Technical Report No. 3 (SC 5117.3TR), Contract N00014-77-C-0441 (July, 1978).

19. H. P. Kirchner, R. C. Garvie, R. M. Gruver and D. M. Richard, "Localized Impact Damage on Transformation Toughened Zirconia," Submitted for publication.

20. F. W. Smith, A. F. Emery and A. S. Kobayashi, "Stress-Intensity Factors for Semicircular Cracks, Part 2 - Semi-Infinite Solid," J. Appl. Mechanics 34 Series E, 953-959 (December, 1967).

21. A. F. Liu, "Stress Intensity Factor for a Corner Flaw," Engineering Fracture Mechanics (4) 175-179 (1972).

22. H. P. Kirchner and R. M. Gruver, "Fractographic Criteria for Subcritical Crack Growth Boundaries in 96% Alumina," To be submitted for publication.

23. R. T. Pascoe and R. C. Garvie, "Surface Strengthening of Transformation-Toughened Zirconia," Ceramic Microstructures (1976) Proceedings of the 6th International Symposium, Richard M. Fulrath, Editor, Westview Press, Boulder, Colo. (1977).

24. J. J. Petrovic, L. A. Jacobson, P. K. Talty and A. K. Vasudevan, "Controlled Surface Flaws in Hot Pressed Si_3N_4," J. Amer. Ceram. Soc. 58 (3-4) 113-116 (1975).

25. R. K. Govilla, "Methodology for Ceramic Life Prediction and Related Proof Testing," Ford Motor Company Interim Report AMMRCTR78-29 (July, 1978).

BASIC DISTRIBUTION LIST

Technical and Summary Reports

Organization	No. of Copies
Defense Documentation Center Cameron Station Alexandria, Virginia 22314	(12)
Office of Naval Research Department of the Navy Arlington, Virginia 22217	
Attn: Code 471	(1)
Code 102	(1)
Code 470	(1)
Commanding Officer Office of Naval Research Branch Office 495 Summer Street Boston, Massachusetts 02210	(1)
Commanding Officer Office of Naval Research Branch Office 536 South Clark Street Chicago, Illinois 60605	(1)
Office of Naval Research San Francisco Area Office 760 Market Street, Room 447 San Francisco, California 94102	
Attn: Dr. P. A. Miller	(1)
Naval Research Laboratory Washington, D.C. 20390	
Attn: Code 6000	(1)
Code 6100	(1)
Code 6300	(1)
Code 6400	(1)
Code 2627	(1)
Naval Air Development Center Code 302 Warminster, Pennsylvania 18974	
Attn: Mr. F. S. Williams	(1)
Naval Air Propulsion Test Center Trenton, New Jersey 08628	
Attn: Library	(1)

Organization	No. of Copies
Naval Construction Batallion Civil Engineering Laboratory Port Hueneme, California 93043	
Attn: Materials Division	(1)
Naval Electronics Laboratory Center San Diego, California 92152	
Attn: Electron Materials Sciences Division	(1)
Naval Missile Center Materials Consultant Code 3312-1 Point Mugu, California 93041	(1)
Commanding Officer Naval Surface Weapons Center White Oak Laboratory Silver Spring, Maryland 20910	
Attn: Library	(1)
David W. Taylor Naval Ship R&D Center Materials Department Annapolis, Maryland 21402	(1)
Naval Undersea Center San Diego, California 92132	
Attn: Library	(1)
Naval Underwater System Center Newport, Rhode Island 02840	
Attn: Library	(1)
Naval Weapons Center China Lake, California 93555	
Attn: Library	(1)
Naval Postgraduate School Monterey, California 93940	
Attn: Mechanical Engineering Dept.	(1)
Naval Air Systems Command Washington, D.C. 20360	
Attn: Code 52031	(1)
Code 52032	(1)
Code 320	(1)

BASIC DISTRIBUTION LIST (Cont'd)

Organization	No. of Copies
Naval Sea System Command Washington, D.C. 20362 Attn: Code 035	(1)
Naval Facilities Engineering Command Alexandria, Virginia 22331 Attn: Code 03	(1)
Scientific Advisor Commandant of the Marine Corps Washington, D.C. 20380 Attn: Code AX	(1)
Naval Ship Engineering Center Department of the Navy CTR BG #2 3700 East-West Highway Prince Georges Plaza Hyattsville, Maryland 20782 Attn: Engineering Materials and Services Office, Code 6101	(1)
Army Research Office Box CM, Duke Station Durham, North Carolina 27706 Attn: Metallurgy & Ceramics Div.	(1)
Army Materials and Mechanics Research Center Watertown, Massachusetts 02172 Attn: Res. Programs Office (AMXMR-P)	(1)
Air Force Office of Scientific Research Bldg. 410 Bolling Air Force Base Washington, D.C. 20332 Attn: Chemical Science Directorate Electronics and Solid State Sciences Directorate	(1) (1)
Air Force Materials Lab (LA) Wright-Patterson AFB Dayton, Ohio 45433	(1)

Organization	No. of Copies
NASA Headquarters Washington, D.C. 20546 Attn: Code RRM	(1)
NASA Lewis Research Center 21000 Brookpark Road Cleveland, Ohio 44135 Attn: Library	(1)
National Bureau of Standards Washington, D.C. 20234 Attn: Metallurgy Division Inorganic Materials Division	(1) (1)
Defense Metals and Ceramics Information Center Battelle Memorial Institute 505 King Avenue Columbus, Ohio 43201	(1)
Director Ordnance Research Laboratory P.O. Box 30 State College, Pennsylvania 16801	(1)
Director Applied Physics Laboratory University of Washington 1013 Northeast Fortieth Street Seattle, Washington 98105	(1)
Metals and Ceramics Division Oak Ridge National Laboratory P.O. Box X Oak Ridge, Tennessee 37380	(1)
Los Alamos Scientific Laboratory P.O. Box 1663 Los Alamos, New Mexico 87544 Attn: Report Librarian	(1)
Argonne National Laboratory Metallurgy Division P.O. Box 229 Lemont, Illinois 60439	(1)

BASIC DISTRIBUTION LIST (Cont'd)

Organization	No. of Copies
Brookhaven National Laboratory Technical Information Division Upton, Long Island New York 11973 Attn: Research Library	(1)
Library Building 50 Room 134 Lawrence Radiation Laboratory Berkeley, California	(1)
Dr. J. D. Buch Prototype Development Assoc., Inc. 1740 Garry Avenue, Suite 201 Santa Ana, CA 92705	(1)
Dr. B. Budiansky Harvard University Department of Engineering and Applied Science Cambridge, MA 02138	(1)
Professor H. Conrad University of Kentucky Materials Department Lexington, KY 40506	(1)
Dr. A. Cooper Case Western Reserve University Materials Department Cleveland, OH 44106	(1)
Dr. I. Finney University of California Berkeley, CA 94720	(1)
Mr. A. A. Fyall Royal Aircraft Establishment Farnborough, Hants UNITED KINGDOM	(1)
Dr. R. Jaffee Electric Power Research Institute Palo Alto, CA	(1)
Dr. L. Rubin Aerospace Corporation P.O. Box 92957 Los Angeles, CA 90009	(1)
Dr. G. Schmidt Air Force Materials Laboratory Wright-Patterson AFB Dayton, OH 54533	(1)
Dr. D. A. Shockey Stnaford Research Institute Poulter Laboratory Menlo Park, CA 94025	(1)
Mr. T. Derkus TRW Cleveland, OH 44117	(1)
Dr. S. Hart Naval Research Laboratory Washington, DC 20375	(1)
Professor G. Kino Stanford University Palo Alto, CA 94305	(1)
Dr. J. Krumhansl Physics Department Cornell University Ithica, NY 14850	(1)
Dr. R. E. Loehman University of Florida Ceramics Division Gainesville, FL 32601	(1)
Dr. D. Mulville Office of Naval Research Code 474 800 North Quincy Street Arlington, VA 22217	(1)
Dr. N. Perrone Office of Naval Research Code 474 800 North Quincy Street Arlington, VA 22217	(1)
Dr. J. R. Rice Brown University Division of Engineering Providence, RI 02912	(1)

SUPPLEMENTARY DISTRIBUTION LIST

Technical and Summary Reports

Organization	No. of Copies
Dr. W.F. Adler Effects Technology Inc. 5383 Hollister Avenue P.O. Box 30400 Santa Barbara, CA 92105	(1)
Dr. G. Bansal Battelle 505 King Avenue Columbus, OH 43201	(1)
Dr. R. Bratton Westinghouse Research Lab. Pittsburgh, PA 15235	(1)
Dr. A.G. Evans Rockwell International P.O. Box 1085 1049 Camino Dos Rios Thousand Oaks, CA 91360	(1)
Mr. E. Fisher Ford Motor Co. Dearborn, MI	(1)
Dr. P. Gielisse University of Rhode Island Kingston, RI 02881	(1)
Dr. M.E. Gulden International Harvester Company Solar Division 2200 Pacific Highway San Diego, CA 92138	(1)
Dr. D.P.H. Hasselman Montana Energy and MHD Research and Development Institute P.O. Box 3809 Butte, Montana 59701	(1)
Mr. G. Hayes Naval Weapons Center China Lake, CA 93555	(1)
Professor A.H. Heuer Case Western Reserve University University Circle Cleveland, OH 44106	(1)
Dr. R. Hoagland Battelle 505 King Avenue Columbus, OH 43201	(1)
Dr. R. Jaffee Electric Power Research Institute Palo Alto, CA	(1)
Dr. P. Jorgensen Stanford Research Institute Poulter Laboratory Menlo Park, CA 94025	(1)
Dr. R.N. Katz Army Materials and Mechanics Research Center Watertown, MA 02171	(1)
Dr. H. Kirchner Ceramic Finishing Company P.O. Box 498 State College, PA 16801	(1)
Dr. B. Koepke Honeywell, Inc. Corporate Research Center 500 Washington Avenue, South Hopkins, MN 55343	(1)
Mr. Frank Koubek Naval Surface Weapons Center White Oak Laboratory Silver Spring, MD 20910	(1)
E. Krafft Carborundum Co. Niagara Falls, NY	(1)

SUPPLEMENTARY DISTRIBUTION LIST (Cont'd)

Organization	No. of Copies
Dr. F.F. Lange Rockwell International P.O. Box 1085 1049 Camino Dos Rios Thousand Oaks, CA 91360	(1)
Dr. J. Lankford Southwest Research Institute 8500 Culebra Road San Antonio, TX 78284	(1)
Library Norton Company Industrial Ceramics Division Worcester, MA 01606	(1)
State University of New York College of Ceramics at Alfred University Attn: Library Alfred, NY 14802	(1)
Dr. L. Hench University of Florida Ceramics Division Gainesville, FL 32601	(1)
Dr. N. MacMillan Materials Research Laboratory Pennsylvania State University College Park, PA 16802	(1)
Mr. F. Markarian Naval Weapons Center China Lake, CA 93555	(1)
Dr. Perry A. Miles Raytheon Company Research Division 28 Seyon Street Waltham, MA 02154	(1)
Mr. R. Rice Naval Research Laboratory Code 6360 Washington, D.C. 20375	(1)
Dr. J. Ritter University of Massachusetts Department of Mechanical Engineering Amherst, MA 01002	(1)
Professor R. Roy Pennsylvania State University Materials Research Laboratory University Park, PA 16802	(1)
Dr. R. Ruh AFML Wright-Patterson AFB Dayton, OH 45433	(1)
Mr. J. Schuldies AiResearch Phoenix, AZ	(1)
Professor G. Sines University of California, Los Angeles Los Angeles, CA 90024	(1)
Dr. N. Tallan AFML Wright-Patterson AFB Dayton, OH 45433	(1)
Dr. T. Vasilos AVCO Corporation Research and Advanced Development Division 201 Lowell Street Wilmington, MA 01887	(1)
Mr. J.D. Walton Engineering Experiment Station Georgia Institute of Technology Atlanta, GA 30332	(1)
Dr. S.M. Widerhorn Inorganic Materials Division National Bureau of Standards Washington, DC 20234	(1)

SUPPLEMENTARY DISTRIBUTION LIST (Cont'd)

Organization	No. of Copies
Dr. S.A. Bortz IITRI 10 W. 35th Street Chicago, IL 60616	(1)
Mr. G. Schmitt Air Force Materials Laboratory Wright-Patterson AFB Dayton, OH 45433	(1)
Dr. Stan Wolf Division of Materials and Science Department of Energy Washington, DC 20545	(1)
Dr. W.G.D. Frederick Air Force Materials Laboratory Wright-Patterson AFB Dayton, OH 45433	(1)
Dr. P. Land Air Force Materials Laboratory Wright-Patterson AFB Dayton, OH 45433	(1)
Mr. K. Letson Redstone Arsenal Huntsville, AL 35809	(1)
Dr. S. Freiman Naval Research Laboratory Code 6363 Washington, DC 20375	(1)
Director Materials Sciences Defense Advanced Research Projects Agency 1400 Wilson Boulevard Arlington, VA 22209	(1)
Dr. James Pappis Raytheon Company Research Division 28 Seyon Street Waltham, MA 02154	(1)
Major W. Simmons Air Force Office of Scientific Research Building 410 Bolling Air Force Base Washington, DC 20332	(1)
Dr. P. Becher Naval Research Laboratory Code 6362 Washington, DC 20375	(1)
Mr. L.B. Weckesser Applied Physics Laboratory Johns Hopkins Road Laurel, MD 20810	(1)
Mr. D. Richarson AiResearch Manufacturing Company 4023 36th Street P.O. Box 5217 Phoenix, AZ 85010	(1)
Dr. H.E. Bennett Naval Weapons Center Code 3818 China Lake, CA 93555	(1)
Mr. G. Denman Air Force Materials Laboratory Code LPJ Wright-Patterson AFB Dayton, OH 45433	(1)
Dr. D. Godfrey Admiralty Materials Laboratory Polle, Dorset BH16 6JU UNITED KINGDOM	(1)
Dr. N. Corney Ministry of Defense The Adelphi John Adam Street London WC2N 6BB UNITED KINGDOM	(1)

SUPPLEMENTARY DISTRIBUTION LIST (Cont'd)

Organization	No. of Copies
Dr. L.M. Gillin Aeronautical Research Laboratory P.O. Box 4331 Fisherman's Bend Melbourne, VIC 3001 AUSTRALIA	(1)
Dr. R. A. Tanzilli General Electric Company Reentry and Environmental Systems Division 3198 Chestnut Street Philadelphia, PA 19101	(1)
Professor John Field University of Cambridge New Cavendish Laboratory Cambridge, UNITED KINGDOM	(1)
Dr. B. R. Lawn Physics Department University of New South Wales Kingston, New South Wales AUSTRALIA	(1)
Mr. W. Trombley Garrett Corporation 1225 Eye Street Washington, D.C. 20006	(1)